Aerodynamic Design of an Aspirated Counter-Rotating Compressor

by

Jody Kirchner

B.A.Sc (Mechanical Eng), University of British Columbia (2000)

Submitted to the Department of Aeronautics and Astronautics
in partial fulfillment of the requirements for the degree of

Master of Science

at the

MASSACHUSETTS INSTITUTE OF TECHNOLOGY

June 2002

Author ....
Department of Aeronautics and Astronautics
May 1, 2002

Certified by.........................
Jack L. Kerrebrock
Professor Emeritus of Aeronautics and Astronautics
Thesis Supervisor

Accepted by...........................
Wallace E. Vander Velde
Professor of Aeronautics and Astronautics
Chair, Committee on Graduate Students

Aerodynamic Design of an Aspirated Counter-Rotating Compressor

by

Jody Kirchner

Submitted to the Department of Aeronautics and Astronautics
on May 1, 2002, in partial fulfillment of the
requirements for the degree of
Master of Science

Abstract

A primary goal in compressor design for jet engines is the reduction of size and weight. This can be achieved by increasing the work output per stage, thereby reducing the required number of stages. In this thesis, the aerodynamic design of a high speed compressor that produces a pressure ratio of 9.1:1 in only two stages (rather than the typical six or seven) is presented. This is accomplished by employing blade aspiration in conjunction with rotor counter-rotation. Aspiration has been shown to make feasible significantly increased blade loading and counter-rotation provides a means of taking full advantage of this potential throughout a multistage compressor.

The aspirated counter-rotating compressor was designed using a one-dimensional stage analysis program coupled with an axisymmetric throughflow code and a quasi-three-dimensional cascade code for blade design. The design of each stage focussed on maximising pressure ratio within diffusion factor and relative inlet Mach number (i.e. shock loss) constraints. The exit angle of the first stator was optimised to maximise the pressure ratio of the counter-rotating (second) rotor. The blade design code MISES allowed for each feature of the blade sections, including aspiration, to be precisely designed for the predicted conditions. To improve the process of designing blades with MISES, extensive analysis of previously designed high-speed aspirated blades was performed to identify the relationships between various blade features.

Thesis Supervisor: Jack L. Kerrebrock
Title: Professor Emeritus of Aeronautics and Astronautics

Acknowledgments

I would like to thank my advisor Professor Jack Kerrebrock for suggesting this project, providing guidance while giving me space to figure things out on my own, and, perhaps most importantly, keeping me excited about the project along the way.

I would also like to thank Ali Merchant for providing supervision and for putting up with my struggles with all the CFD programs. Also, thanks for writing an excellent PhD thesis which was an invaluable reference for this work. Thanks to Brian Schuler for teaching me how to use MISES and for providing assistance along the way.

Finally, a very special thanks to all the friends I have made at MIT who have helped make this a great experience.

Contents

List of Figures

List of Tables

Chapter 1

Introduction

1.1 Motivation and Background

A driving force in compressor design is the desire to achieve a high pressure ratio and efficiency while maintaining or decreasing the size (particularly length) and weight of the compressor. It is also beneficial to reduce the number of parts, especially blades which are expensive to produce and maintain. To this end it is necessary to develop means of improving the performance of individual compressor stages so that fewer stages are required for a given application.

The pressure ratio attainable in a compressor stage has traditionally been limited by viscous effects on the blades, in particular flow separation. However, recent work by Kerrebrock and others has shown that removing a portion of the boundary layer fluid from the blade surface through aspiration can delay separation and allow for significantly increased blade loading (see for example [11], [12]). This in turn reduces the number of stages required to obtain the desired compressor pressure ratio. A low-speed compressor stage employing aspiration has been built and tested successfully [18, 21] and a high-speed stage has been designed and is under construction for testing [18]. With aspiration shown to be viable way of raising the loading limits of blades, it is an opportune time to consider means of taking advantage of the ability to do more work with each stage.

A conventional compressor stage consists of a rotating blade row, or rotor, and a stationary blade row, or stator. The rotor does work on the fluid given by

$$W_R = \omega(r_2 v_2 - r_1 v_1) \tag{1.1}$$

where ω is the angular velocity and rv is the angular momentum per unit mass (also called swirl) at the inlet (1) and exit (2). The stator converts some fraction of the rotor work into a static pressure rise. Equation 1.1 shows that there are two ways to increase the work of a stage: increase the tip speed and increase the change in swirl or turning. However, tip speed in modern compressors is limited by structural constraints, so increased turning must be considered as a means to obtain any increase in work.

There is a wide range of design options to choose from in selecting the swirl at the inlet to the rotor, $r_1 v_1$, but in modern high-work compressors the stators typically remove all of the swirl from the upstream rotors, so that the flow entering each rotor is axial ($r_1 v_1 = 0$). Even with advances in blade design, there is a limit on how far the rotor can turn the flow from the axial direction and, therefore, how much work it can do on the flow. However, if the flow entering the rotor has swirl against the direction of rotation ($r_1 v_1 < 0$), for the same rotor exit angle the amount of work is increased. This can be achieved throughout a multistage compressor by reducing the turning of the stators (or removing the stators altogether) and alternating the direction of rotation of the spools. This is termed counter-rotation.

Figure 1-1 shows the ratio of the ideal work output of a simple two-stage counter-rotating compressor to that of a conventional two-stage compressor given by

$$\frac{W_{counter}}{W_{co}} = \frac{\omega r(v_c - v_b)_{counter}}{\omega r(v_c - v_b)_{co}} = 1 + \frac{1}{2}\tan\alpha \tag{1.2}$$

where α is the exit angle of the first stator for the counter-rotating configuration. Geometrically, the configurations are identical except for the exit angle of the first stator which is zero for the conventional configuration and varies for the counter-rotating configuration. This simple analysis shows that a significant increase in work is possible with counter-rotation.

A more extensive assessment of the performance improvement possible for a single compressor stage with inlet counter-swirl was made by Law and Wennstrom [14].

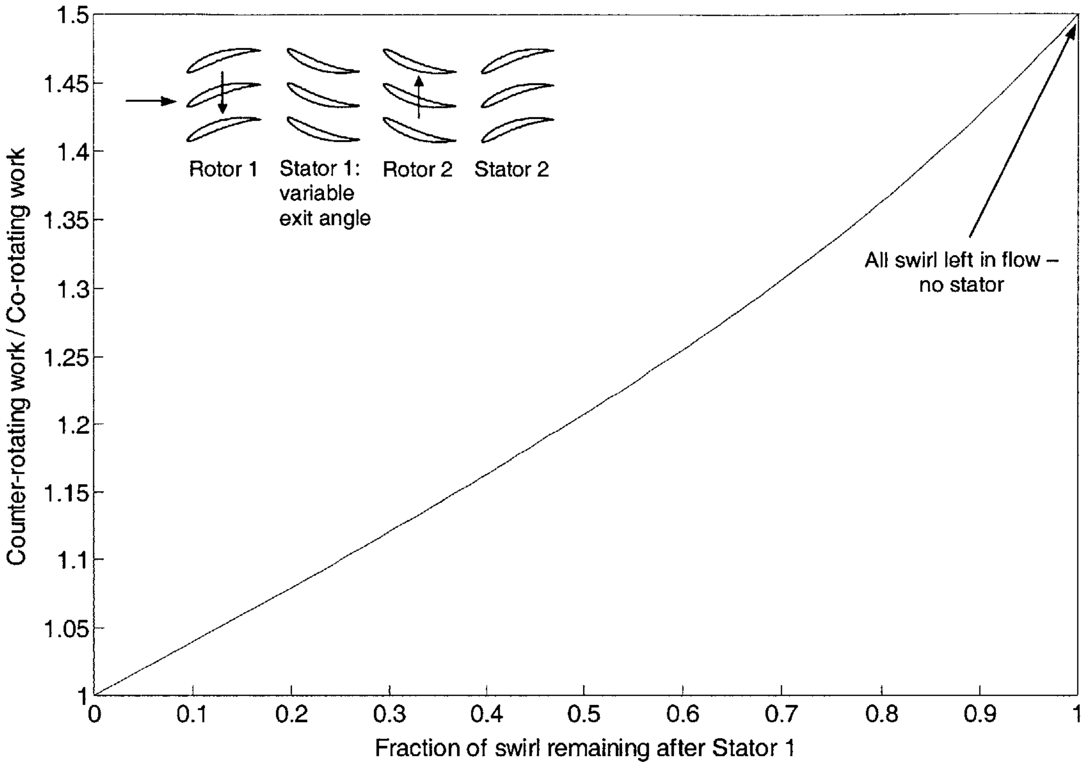

Figure 1-1: Work output of counter-rotating relative to conventional compressor

They designed and tested a stage with counter-swirl imparted by inlet guide vanes. With a tip speed of 1500ft/sec the rotor successfully achieved a pressure ratio of 2.42 at a peak isentropic efficiency of 91.6%. The stage pressure ratio and isentropic efficiency were 2.30 and 85.8% respectively.

The use of counter-rotation in previous compressor designs has not resulted in such a considerable improvement. Since the feasible increase in blade loading has been restricted by viscous effects, a large number of stages have still been required. However, mechanical limitations make possible the application of counter-rotation between only a few stages, so the overall impact on performance has been low. However, in a compressor with few stages (two or three), such as would be feasible with aspirated blades, the benefits of counter-rotation can be captured by each stage without an unrealistically large number of spools. Therefore there is an opportunity for significant performance improvement if aspiration and counter-rotation are utilised together.

Preliminary work was done at MIT by Freedman to determine the best configuration for an aspirated counter-rotating compressor and for the engine in which it would operate [9]. Several compressor configurations involving different combinations of rotors and stators were investigated, but it was concluded that a conventional rotor-stator configuration was optimal. Attempts to maximise the residual swirl and minimise the compressor length by removing the stators resulted in unacceptably high Mach numbers and losses in the rotors. The compressor and engine configuration that was developed previously is shown schematically in Figure 1-2 along with a conventional modern engine with the same pressure ratio for comparison. The decrease in the length of the engine made possible by increasing the work output per stage via counter-rotation and aspiration is significant.

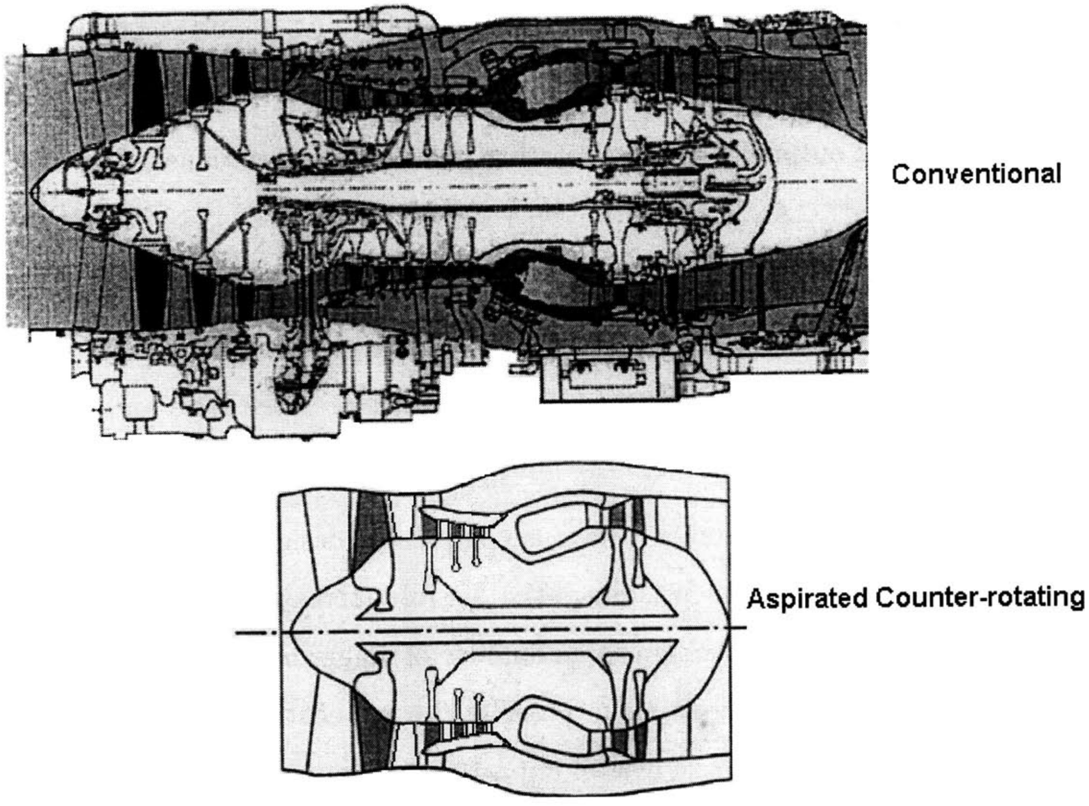

Figure 1-2: Conventional modern engine and conceptual engine with aspirated counter-rotating compressor (adapted from Reference [8])

1.2 Objectives

The purpose of this work was to continue with the development of the multi-stage aspirated counter-rotating compressor discussed in Section 1.1. More specifically, the primary goal was to produce a detailed aerodynamic design of a two-stage compressor to be tested in the Blowdown Compressor facility at MIT. These tests will be used to assess the validity of the aspirated counter-rotating concept for use in practical applications.

Although other applications are possible, it is presently thought that an aspirated counter-rotating compressor would be ideal for use as a core compressor in a long range supersonic cruise aircraft. This is mainly because such aircraft are especially sensitive to weight. This foreseen application provided the basis for many of the parameters of the current design.

1.3 Outline

The body of this thesis details the steps and results of the compressor design. Chapter 2 provides a theoretical background for the work, including the important parameters and equations for the stage analysis and evaluation of losses and aspiration. The steps of the design process as well as the goals and constraints are presented in Chapter 3. Chapter 4 discusses the design of the compressor stages and the flowpath including the work distribution and geometry choices. The results of a computational throughflow analysis are also presented in this chapter. Chapter 5 describes the design of the blade sections using a quasi-three-dimensional turbomachinery cascade code and presents the final blade designs. Finally, Chapter 6 provides some conclusions, including a summary of the compressor design as well as a discussion of future work.

Chapter 2

Compressor Theory

2.1 Stage Analysis

In a one-dimensional compressor stage analysis, the flow through a blade row (rotor and stator) is described by the changes in velocity components as shown in Figure 2-1. The components shown as solid vectors represent absolute velocities and those shown as dotted vectors represent velocities relative to the rotating frame of reference of the rotor. The conditions at the stage inlet (denoted with the subscript 1) are known either from the compressor inlet conditions (for the first stage) or the upstream stage exit conditions (for subsequent stages). To simplify the analysis, it is often assumed that the axial velocity, w, is constant, although in reality it will fluctuate across the blade rows.

The change in tangential velocity, v, across the rotor can be related to the stagnation temperature, T_t, rise by the Euler equation

$$c_p(T_{t2} - T_{t1}) = \omega(r_2 v_2 - r_1 v_1) \tag{2.1}$$

where ω is the rotational speed, r is the radius, and c_p is the specific heat at constant pressure. In the design problem considered here, the stagnation temperature change is fixed by the desired pressure ratio and the required tangential velocity change must be found. The pressure ratio

$$\pi \equiv \frac{P_{t2}}{P_{t1}} \tag{2.2}$$

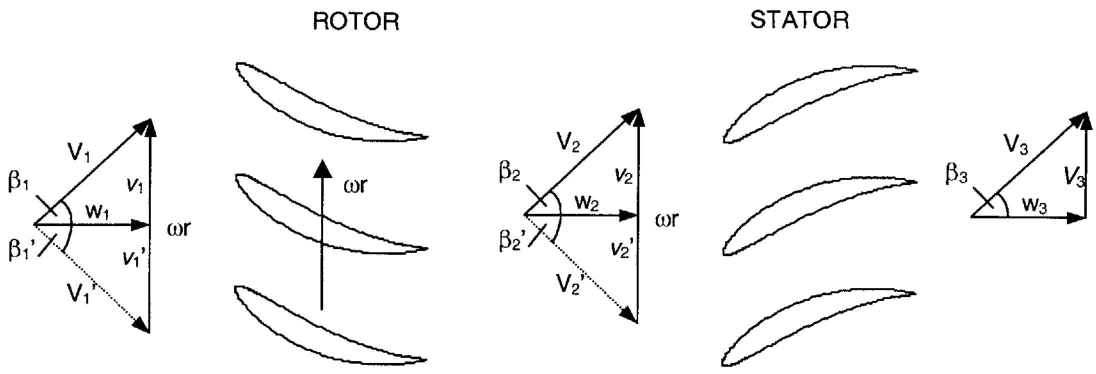

Figure 2-1: Compressor stage nomenclature

and temperature ratio

$$\tau \equiv \frac{T_{t2}}{T_{t1}} \tag{2.3}$$

are related by the efficiency of the stage, η, which is the ratio of the ideal work of the blade row to the actual work required to give the desired pressure ratio. The efficiency is affected by entropy losses due to viscous shear forces, shocks, etc. In a simplified stage analysis, a value of efficiency is assumed at the start so that the temperature ratio can be found from

$$\tau = 1 + \frac{\pi^{(\gamma-1)/\gamma} - 1}{\eta} \, . \tag{2.4}$$

where γ is the ratio of specific heats.

With the required tangential velocity downstream of the rotor known from the Euler equation, the other velocity components at this position can be found from geometry. The relations are

$$v_2{}' = w - v_2 \, , \tag{2.5}$$

$$V_2 = \sqrt{w^2 + v_2{}^2} \, , \qquad V_2' = \sqrt{w^2 + v_2'^2} \, , \tag{2.6}$$

$$\beta_2 = \arctan\left(\frac{v_2}{w}\right) \, , \qquad \text{and } \beta'{}_2 = \arctan\left(\frac{v_2'}{w}\right) \, . \tag{2.7}$$

The primed values are relative to the rotor frame of reference.

The flow through the stator involves only diffusion without energy addition and generally the exit angle of the stator is a flexible design parameter. It is chosen based on the inlet flow desired for the downstream component, within the aerodynamic constraints of the blade (for example, the separation characteristics). Once the stator exit angle is chosen, the velocity components at that position can be found from

$$v_3 = w \tan \beta_3 \ , \text{ and} \tag{2.8}$$

$$V_3 = \sqrt{w^2 + {v_3}^2} \ . \tag{2.9}$$

Generally, it is useful to represent the velocities through the compressor as Mach numbers given by

$$M = \frac{V}{a} \ . \tag{2.10}$$

The quantity a is the local speed of sound

$$a = \sqrt{\gamma R T} = \sqrt{\gamma R \left(T_t - \frac{V^2}{2c_p} \right)} \tag{2.11}$$

where R is the specific gas constant, and T is the static temperature.

For a counter-rotating compressor stage, the analysis is the same as that for a conventional stage except that the tip speed used in the Euler equation is negative. When determining the velocity components geometrically, care must be taken to use tangent and sine functions rather than cosine so that the negative relative velocities are preserved.

2.2 Dimensionless Parameters

From the quantities obtained in the stage analysis, several useful dimensionless parameters can be defined, in addition to the pressure and temperature ratios. These dimensionless parameters are useful in summarising a compressor design since values for different compressors can be compared more directly than can dimensional parameters.

The work done across the stage, $c_p \Delta T_t$, and the rotor speed, ωr, are combined to give the stage loading coefficient which is a measure of the fraction of blade energy transferred to the fluid

$$\psi = \frac{c_p \Delta T_t}{(\omega r)^2} \ . \tag{2.12}$$

The axial velocity, w, and the rotor speed are combined to give the flow coefficient

$$\Phi = \frac{w}{\mid \omega r \mid} . \tag{2.13}$$

The absolute value of the rotational speed is used here so that the flow coefficient will be positive for the counter-rotating rotor. The distribution of loading in the stage is represented by the degree of reaction which is the ratio of the static enthalpy, $c_p T$, rise in the rotor to that in the stage

$$^o\!R_c = \frac{T_2 - T_1}{T_3 - T_1} . \tag{2.14}$$

The fractional change in axial velocity through a blade row is termed the axial velocity ratio

$$\mathrm{AVR} = \frac{w_2}{w_1} . \tag{2.15}$$

This value is important to blade boundary layer behaviour which depends heavily on whether the flow is accelerating (AVR > 1) or decelerating (AVR < 1). In the stage analysis described in Section 2.1, the axial velocity ratio will be equal to one (since axial velocity is assumed constant), but this will not in general be the case. For flow in which large density changes occur, such as in high-speed compressors, a more useful parameter is the axial velocity density ratio

$$\mathrm{AVDR} = \frac{\rho_2 w_2}{\rho_1 w_1} \tag{2.16}$$

which represents the streamtube contraction or expansion through the blade row.

2.3 Losses

In low-speed compressors the most significant source of loss is viscous shear on the blades. However, for high-speed compressors, such as that considered here, shock losses can be up to seven or eight times larger than viscous losses (as seen with the aspirated blades designed by Merchant [18]). Therefore, an accurate model for both types of loss is important. More minor sources of loss such as tip leakage losses and possible shroud losses are not considered here.

To avoid results that are dependant on the frame of reference (moving for the rotor and stationary for the stator), the losses are presented in terms of the resulting entropy increase in the flow, Δs [10]. The entropy rises due to each component of loss for the rotor and stator can be added to give the total entropy increase for the stage. The entropy rise and temperature ratio of the stage give the adiabatic efficiency

$$\eta = \frac{\tau e^{\Delta s_{total}/c_p} - 1}{\tau - 1} \ . \tag{2.17}$$

2.3.1 Viscous Losses

Viscous losses in cascades are represented by a non-dimensional pressure loss coefficient

$$\bar{\omega} = \frac{\Delta P_t}{P_{t1} - P_1} \ . \tag{2.18}$$

Analysis of cascade data by Lieblein [15] lead to a correlation between the loss coefficient and the now widely used diffusion factor which is a measure of the deceleration of the flow through the blade passages. The diffusion factor is given by

$$D = 1 - \frac{V_2}{V_1} + \frac{|v_2 - v_1|}{2\sigma V_1} \tag{2.19}$$

where the subscript 1 represents relative inlet flow and the subscript 2 represents relative exit flow. The solidity of the cascade, σ, is the ratio of the chord length to the blade spacing. Figure 2-2 shows the Lieblein correlation between the loss parameter which is a function of the loss coefficient and the diffusion factor

$$\bar{\omega} \frac{\cos \beta_2^2}{\cos \beta_1^2} \frac{\cos \beta_2}{2\sigma} = f(D) \ . \tag{2.20}$$

For low diffusion factors (below about 0.45) the viscous loss is almost constant, but above this value the loss increases rapidly due to boundary layer separation. For this reason, conventional blades are generally limited to diffusion factors well below 0.5.

Adding aspiration to blades reduces the boundary layer thickness. Therefore, it is possible to go to higher diffusion factors before approaching separation and incurring a rapid increase in loss. Schuler [21] presents a correlation between the diffusion factor and the loss parameter for aspirated blades, similar to Lieblein's correlation for conventional blades. This is also shown in Figure 2-2.

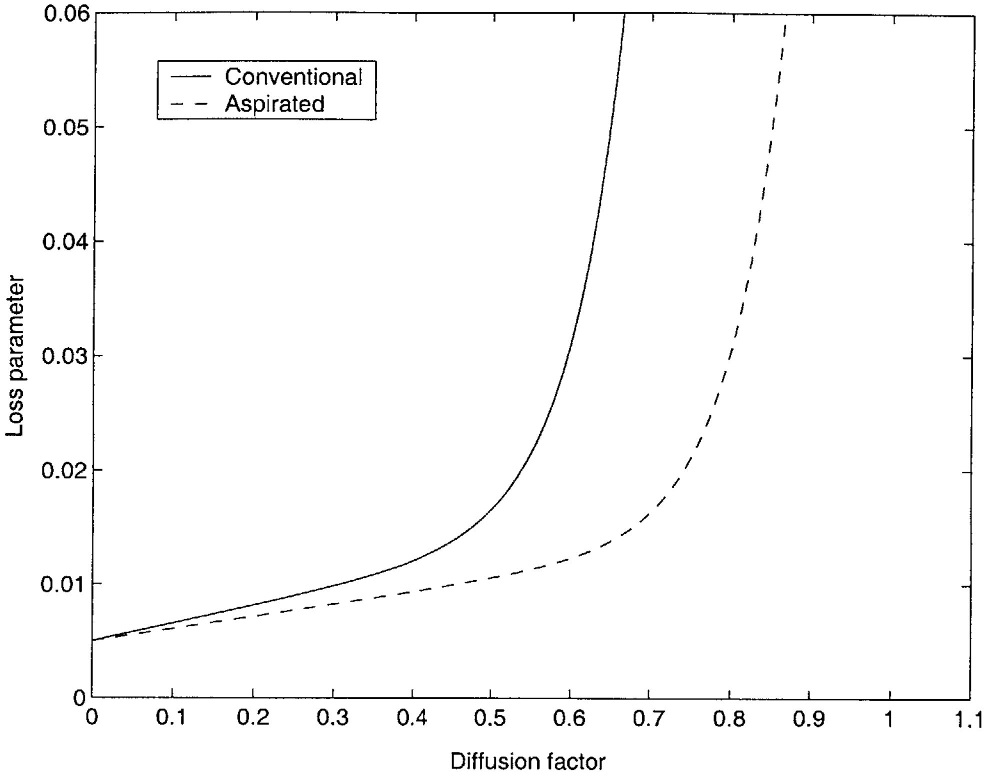

Figure 2-2: Correlation of diffusion factor and loss parameter

Once the diffusion factor for a blade row has been determined from the velocities using Equation 2.19, the loss coefficient can be found from Figure 2-2 or from relationships derived from these curves (for example, see Reference [21]). The entropy rise corresponding to the loss coefficient is

$$\Delta s_{viscous} = -R\ln\left(1-\bar{\omega}\left(1-\frac{P_2}{P'_{t2}}\right)\right) \tag{2.21}$$

where the stagnation pressure, P'_{t2}, is relative to the frame of reference moving with the blade row.

2.3.2 Shock Losses

Although shock losses have a significant impact on the performance of supersonic compressors, the models available are not as well established as those for viscous losses. Kerrebrock [10] suggests that the shock loss for a blade row be estimated as the average of the loss due to a normal shock at the relative inlet Mach number and the loss due to a normal shock at the suction surface impingement location Mach number. Experimental data has shown that the actual shock losses in rotors are lower than predicted by this method, so it provides a conservative estimate.

The blade relative Mach number will be known from the stage analysis, but the shock impingement Mach number must be estimated since the position of the shock will not generally be known at this point in the design. Based on aspirated blades designed by Merchant, Schuler [21] presents an equation to estimate the shock impingement Mach number,

$$M_{imp} = 1.225 M_{rel} \ . \tag{2.22}$$

With the Mach numbers known, the corresponding entropy rise through the shock is

$$\Delta s_{shock} = c_p \ln\left(\left(1+\frac{2\gamma}{\gamma+1}(M^2-1)\right)\left(\frac{2+(\gamma-1)M^2}{(\gamma+1)M^2}\right)\right) - R\ln\left(1+\frac{2\gamma}{\gamma+1}(M^2-1)\right) \ . \tag{2.23}$$

The average of the entropy rises at the two Mach numbers provides the entropy rise for the blade row.

The relationship between blade relative inlet Mach number and entropy rise due to shock loss (normalised by c_p) is plotted in Figure 2-3. From the plot it is evident that above a relative inlet Mach number of about 1.5, losses begin to rise quickly above the low values seen at transonic Mach numbers. This is a useful guideline for supersonic compressor stage design.

2.4 Aspiration

Aspiration of a compressor blade involves removing some of the boundary layer fluid from the blade surface. The fluid is generally removed through a slot in the surface just ahead of a region of rapid pressure rise, often a shock impingement location. The effect is that the boundary layer growth is hindered and therefore separation is delayed. As shown in Section 2.3.1 this increases the diffusion limit for the blade, so that more work can be done for a given blade speed without incurring large losses. Aspiration is also thermodynamically beneficial since it removes high-entropy fluid from the flow.

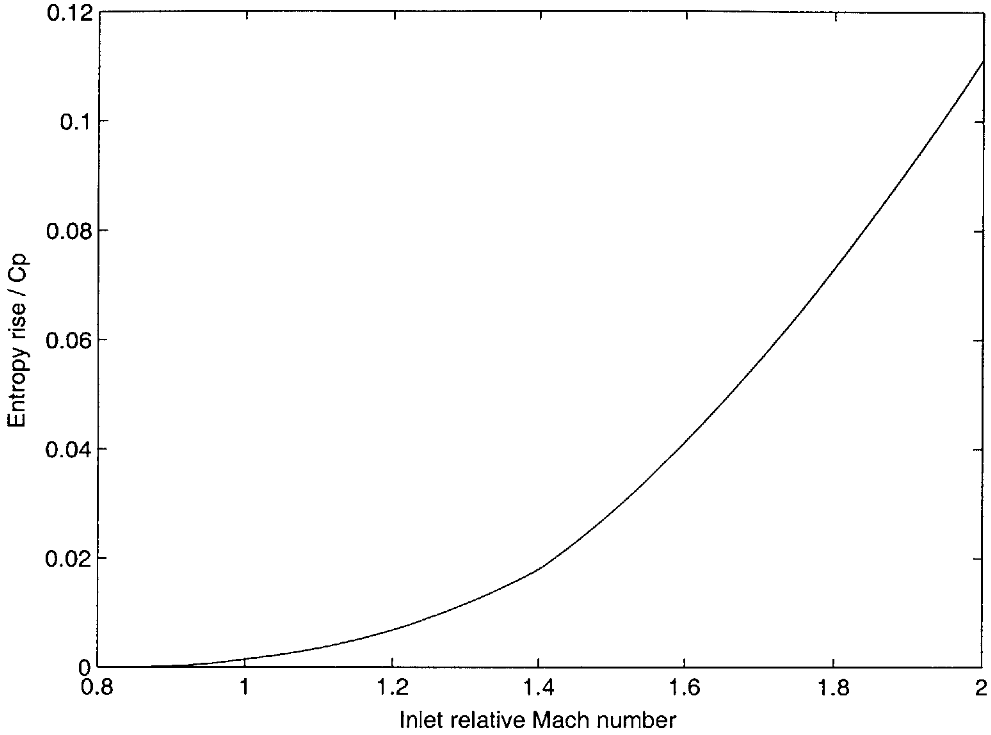

Figure 2-3: Variation of entropy rise due to shock loss with inlet Mach number

A schematic of a typical suction slot is shown in Figure 2-4. The most important features are the mass flux of fluid removed and the location and length of the suction slot. The effect of the mass removal can be represented by the resulting decrease in boundary layer displacement thickness

$$\delta^*_{suct} = -\int_{s_1}^{s_2} \frac{\rho_w v_w}{\rho_e u_e} ds \tag{2.24}$$

where $(s_2 - s_1)$ is the length of the suction slot and $\rho_w v_w$ is the normal mass flux into the slot. The ratio of the displacement length due to suction to the upstream displacement thickness of the boundary layer, δ^*_1, provides a measure of the effectiveness of the aspiration in decreasing the momentum and displacement thicknesses.

The displacement thickness ratio is used to define the suction coefficient which gives the suction mass flow as a fraction of the inlet flow

$$c_m \equiv -\frac{1}{\dot{m}_{in}} \int_{s_1}^{s_2} \rho_w v_w ds = \left(\frac{\delta^*_{suct}}{\delta^*_1}\right) \left(\frac{Re_{\theta 1}}{Re_c}\right) H_1 \sigma \tag{2.25}$$

where $Re_{\theta 1}$ is the upstream momentum thickness Reynolds number, Re_c is the freestream

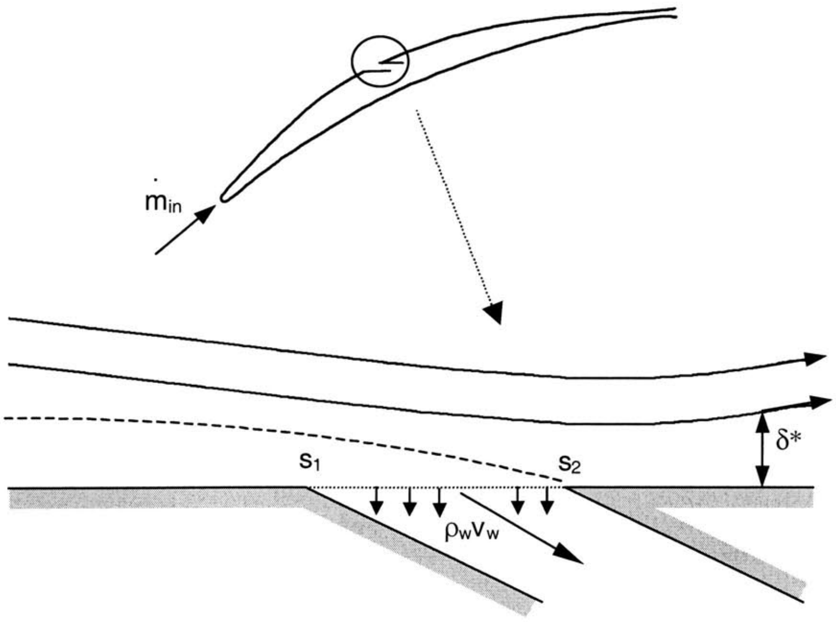

Figure 2-4: Suction slot (adapted from Reference [18])

Reynolds number based on chord length, H_1 is the boundary layer shape parameter, and σ is the solidity of the blade row [18].

The effect of aspiration on the growth of a typical boundary layer on a high-work supersonic rotor blade is illustrated in Figure 2-5 [18]. Without suction the overall loss of the blade is 3 times higher than with suction and the viscous loss is 10 times higher.

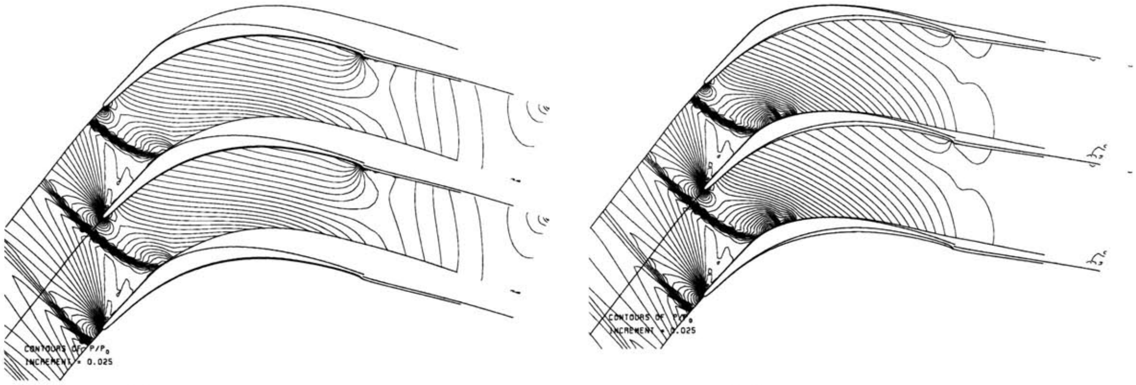

(a) Without aspiration (b) With aspiration

Figure 2-5: Effect of aspiration on a blade boundary layer [18]

Chapter 3

Design Methodology and Objectives

3.1 Design Process

The design process followed in this work was adapted from that used by Merchant [18] to design low- and high-speed aspirated compressor stages. The process is outlined schematically in Figure 3-1.

Given a set of goals and constraints for the compressor, the first step in the design process is to determine the required flow properties upstream and downstream of each stage, including the flow angles and velocities. From this information the flowpath and axial blade geometry can be generated. The geometry and the parameters from the stage design are then input to an axisymmetric throughflow solver which provides more detailed aerodynamic information. The throughflow solver also outputs the data required for the quasi-three-dimensional design of the blades which is performed in the next step. Finally a complete three-dimensional analysis of the design is performed. After each step, the new (and presumably improved) information gained is input to the previous step to refine the design. This leads to an iterative process for which the final goal is agreement between the results from each analysis and satisfaction of the constraints of the problem. This thesis carries the design only through the quasi-three-dimensional design phase.

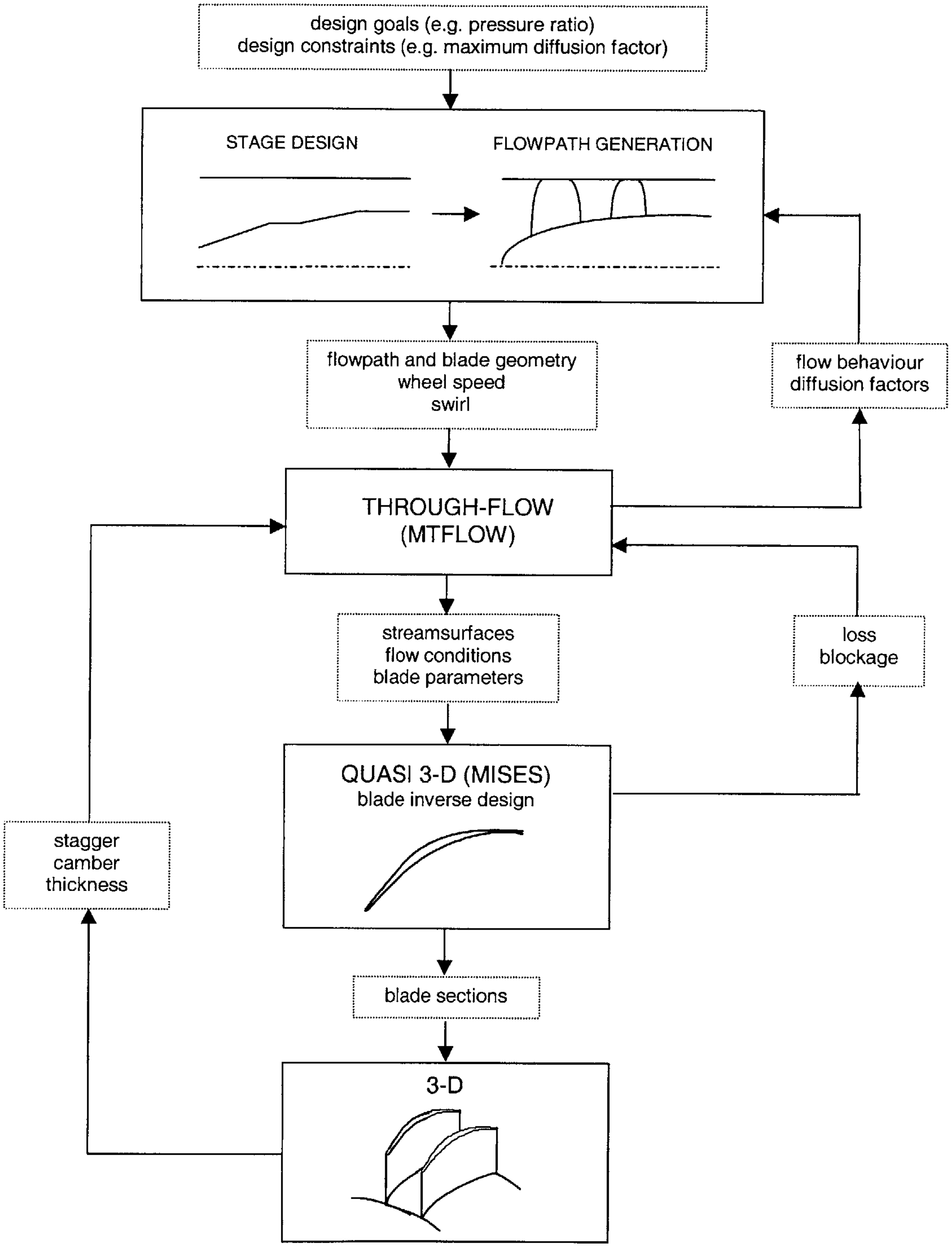

Figure 3-1: Compressor design process

3.2 Goals and Constraints

The main goal of this work was to design a compressor that will be used in experiments to assess the use of counter-rotation together with aspiration. Based on this intended application and on past compressor designs several parameters of the design were fixed or constrained to be within certain limits. These values are summarised in Table 3.1.

Number of stages	2
Total pressure ratio, π	10
Inlet Mach number, M_a	0.65
Maximum tip speed, U_{tip}	457m/sec (1500ft/sec)
Minimum inlet hub/tip ratio	0.5
Maximum diffusion factor	0.7
Maximum (blade) relative inlet Mach number	1.5
Maximum solidity	3.5

Table 3.1: Design goals and constraints

The pressure ratio goal for the compressor was 10:1 in two stages. This was determined to be feasible based on past work on the aspirated counter-rotating compressor and on aspirated compressor stages. To obtain this pressure ratio, the tip speed of the compressor was chosen to be the maximum possible within structural limitations. A high tip speed and pressure ratio are consistent with the expected application of the counter-rotating compressor as a core compressor. The inlet Mach number of 0.65 is also a typical core compressor value.

The inlet hub-to-tip radius ratio was constrained by the requirements of the experimental setup. Namely, the fact that the motor to drive the first stage will likely be located below the hub casing at the compressor inlet. As discussed in Section 2.3.1, the maximum allowable diffusion factor for the aspirated blades was determined based on previous work. For diffusion factors higher than 0.7 it is expected that viscous losses will increase rapidly. Likewise, the relative inlet Mach number should be below

1.5 to avoid large shock losses. Finally, the maximum solidity requirement exists to limit the number of blades required and help avoid blockage problems. The value of 3.5 was chosen based on past experience and is at the high end of the typical range so as to help keep diffusion losses low.

Chapter 4

Stage and Flowpath Design

The first step in the design process was to quantify the properties of each stage, including the geometry, flow angles, Mach numbers, and losses, based on the given values and constraints. Many of the design variables were unconstrained so some investigation of previous designs and experimentation was required to find the best combination of parameters. Once the stage properties were fixed, the flowpath was generated and a throughflow CFD code was used to analyse the design. This process was repeated until the throughflow results were acceptable.

4.1 Stage Analysis

To design the stages, a simple stage analysis program was developed with the procedure described in Section 2.1 implemented at three spanwise locations: hub, mean, and tip. Radial equilibrium was assumed. The diffusion factors and viscous and shock losses were also computed using the models discussed in Section 2.3. This program facilitated the relatively quick investigation of many design alternatives and hence allowed for some rudimentary design optimization. The primary metric used to determine the best design at this step was the distribution of diffusion factors. However, consideration was also given to the relative Mach numbers entering the blade rows, since shock losses were expected to be significant.

4.1.1 Work Distribution

A primary goal of the stage design was to fix the pressure ratio or work division for the stages. For ease of design, the pressure ratio of the first stage was chosen to match that of the high-speed aspirated stage designed by Merchant [18]. The design of this stage, including the blade sections, has been completed successfully. The pressure ratio of the second stage was then fixed by the overall compressor requirement. The required pressure ratios of the rotors were initially estimated using an assumed pressure ratio for the stators. This was revised when more accurate values were available from the throughflow analysis.

4.1.2 Interstage Swirl

The swirl distribution (rv) at the exit of the first stator is critical to the design since it directly determines the usefulness of the counter-rotation. However, determining the optimum distribution was not straightforward as several competing design variables are influenced by the swirl, including the diffusion factors at several locations. Clearly, maximizing the swirl entering the second stage maximizes the benefit of counter-rotation. The pressure ratio of the second rotor can be increased while decreasing the diffusion factors of both stators. However, the residual swirl increases the relative Mach number entering the second rotor, thereby increasing the shock losses. The swirl also increases the reaction of the second stage meaning that the rotor shares a larger burden in producing the enthalpy rise in the stage. The diffusion factor of the second rotor is affected by the swirl as well, but the relationship is relatively complicated as it depends on the radial location. This is illustrated in Figure 4-1.

A preliminary investigation of the effects of the stator swirl distribution (as discussed above) was completed with the stage analysis program. However, there were secondary effects of the distribution that were only evident in the throughflow solution. These effects were more complicated and not easy to quantify. Therefore, iteration on this feature of the design using the throughflow code was necessary.

The stator swirl distribution that was selected is shown graphically in Figure 4-2.

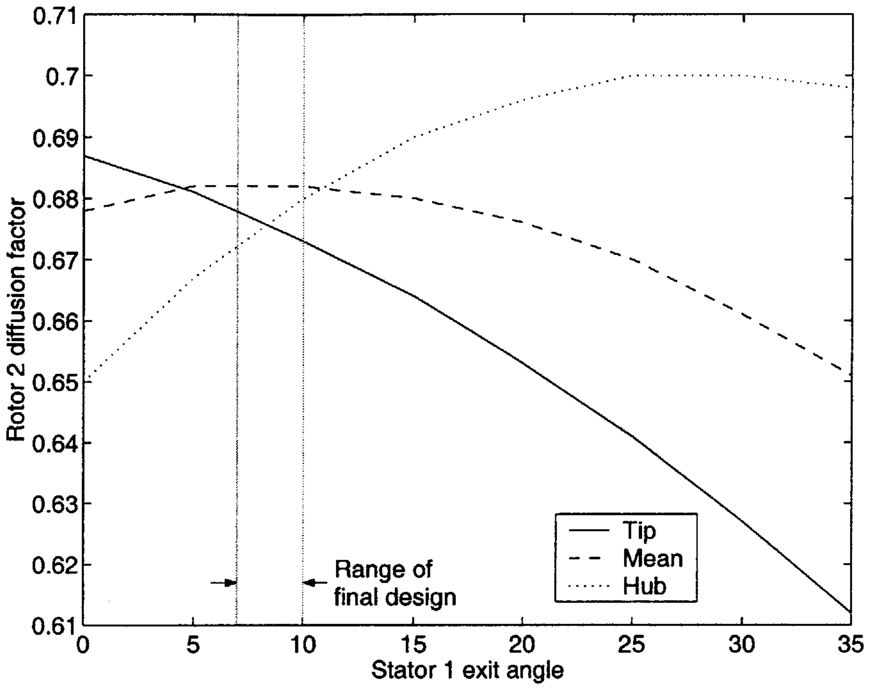

Figure 4-1: Variation of rotor 2 diffusion factor with inlet swirl

It is characterised by approximately constant angles in the vicinity of the hub and tip and a linear variation between to give a roughly s-shaped distribution. The maximum angle is about 10 degrees near the tip and the minimum is about 7 degrees near the hub which puts the distribution within the ideal range for minimising the diffusion factors of the second rotor as shown in Figure 4-1[1]. The maximum exit angle of 10 degrees also ensures that the relative tip Mach number of the downstream rotor is not much higher than 1.5. Although this angle distribution was chosen to give the best aerodynamic results, it is also beneficial from a structural standpoint since the stator trailing edge is closer to being perpendicular to the wall at the hub and tip than would be the case for a linear distribution, for example.

---

[1] The final diffusion factors determined with the throughflow code were higher than those predicted here, but the trend was correct

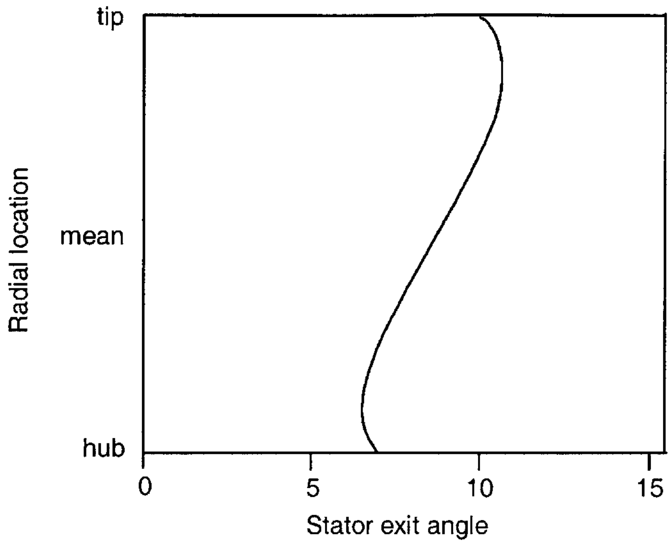

Figure 4-2: Stator 1 exit angle distribution

4.1.3 Geometry

Once the flow properties across each blade row were fixed, an estimate of the required area variation was found using a modified form of the corrected mass flow equation also used by Freedman [9],

$$\frac{A_2}{A_1} = \frac{P_{t1}}{P_{t2}}\sqrt{\frac{T_{t2}}{T_{t1}}}\frac{M_{x1}}{M_{x2}}\frac{\left(1+\frac{\gamma-1}{2}{M_2}^2\right)^{\frac{\gamma+1}{2(\gamma-1)}}}{\left(1+\frac{\gamma-1}{2}{M_1}^2\right)^{\frac{\gamma+1}{2(\gamma-1)}}} \tag{4.1}$$

where M_x is the axial Mach number. The use of the total rather than axial Mach number in the last term is a simple — although not completely accurate — means of taking into account the effect of swirl. The actual area change that is found by solving differential equations of motion for swirling flow (such as those presented by Anderson, Heiser and Jackson [2]) is generally smaller than that found with Equation 4.1 so a correction must be applied. This was determined iteratively using the solution from the throughflow computations, particularly the axial velocity density ratio (Equation 2.16). The value of the axial velocity density ratio should be around one at the hub.

The blade heights were fixed by the compressor throughflow area (neglecting the tip clearance required for the rotor), but the chord lengths and solidities were among the unconstrained design variables. For all of the blade rows, the hub solidity was set close to the maximum allowable value to keep the diffusion factors low. Approximately constant chord lengths were used for all blade rows to maximize the solidities away from the hub. The values of the chord lengths were determined from the aspect ratios. These were chosen based on other modern high-speed core compressor designs.

4.2 Flowpath Generation

The large pressure ratios across each stage in this design necessitate area contractions that are much larger than typically seen in axial compressors. This made the flowpath design particularly challenging. Frequently, axial compressors are designed with a constant tip radius which means only the hub is contoured to achieve the required area variation. This minimizes the turning required for a given rate of rotation (because the radii are kept high) and helps keep the losses low. Also, the possibility of the rotor hitting the tip casing during forward-backward vibration is virtually eliminated. However, if the required area contractions are large a constant tip radius leads to a very convoluted profile at the hub. This can adversely affect the flow behavior and increase the structural complexity. Also, there is some benefit to decreasing the tip radius in that it accelerates the flow at the tip and decreases the diffusion factors there. Therefore, for this design a linearly decreasing tip radius was used. The angle of the tip casing relative to the rotational axis is about 3^o.

Approximate radial coordinates for the hub were determined from the required area (found using Equation 4.1) upstream and downstream of each blade row. Axial coordinates were determined by taking axial projections of the blades and assuming a blade row separation distance of one-quarter of the maximum chord length of the upstream blade as suggested by Mattingly [16]. The cubic spline package in MATLAB [2] was used to interpolate between the hub points and generate a smooth flowpath. A major objective in this process was to avoid sharp curves so as to reduce the possibility of flow separation and minimize the pressure gradients caused by streamline curvature. Across the rotors the hub was constrained to be linear to avoid mechan-

---

[2] See MATLAB documentation at www.mathworks.com

ical complexity. The linear tip radius decrease lead to a hub ramp angle at the first rotor of about 30^o. For the subsequent blade rows, the hub ramp angle decreases approximately linearly.

After the flowpath was initially generated, it was optimised using the results of the throughflow computations (discussed in the next section). This primarily involved further smoothing of the hub profile and small area changes based on the computed axial velocity density ratios. The final flowpath with the axial blade projections is shown in Figure 4-3.

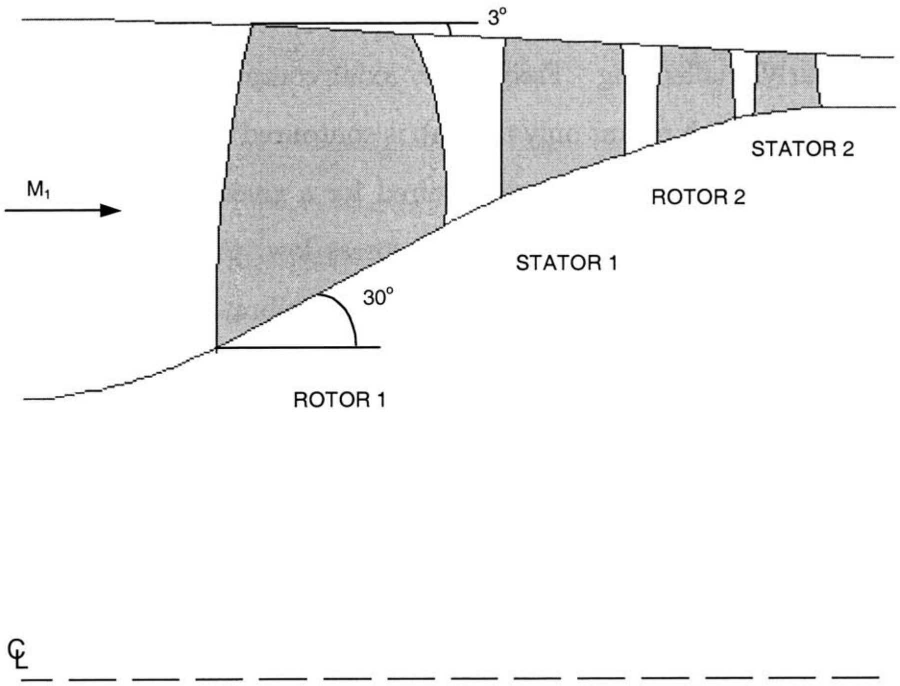

Figure 4-3: Flowpath and blades

4.3 Throughflow Analysis

To obtain more accurate estimates for the compressor performance (and improve the design where necessary), the results of the stage design were analysed with a throughflow CFD code. This code was also used to generate the input files for the blade design.

4.3.1 Code Description

The throughflow analysis was performed with MTFLOW, an axisymmetric code developed at MIT by Drela [5]. MTFLOW solves the Euler equations on a streamline grid taking into account the effects of swirl, loss generation, and blockage which are input as spanwise distributions. End wall boundary layers, spanwise mixing, and non-axisymmetric effects are not modelled in the code.

For reference, the 3-D Euler equations in vector form are

$$\frac{\partial \vec{U}}{\partial t} + \frac{\partial \vec{F}}{\partial x} + \frac{\partial \vec{G}}{\partial y} + \frac{\partial \vec{H}}{\partial z} = \rho \vec{Q} \tag{4.2}$$

where U is the state vector, F, G, and H are the flux vectors in the x, y, and x directions respectively, and Q is the source term for centrifugal and Coriolis forces,

$$\vec{U} = \begin{pmatrix} \rho \\ \rho u \\ \rho v \\ \rho w \\ \rho E \end{pmatrix} , \tag{4.3}$$

$$\vec{F} = \begin{pmatrix} \rho u \\ \rho u^2 + p \\ \rho u v \\ \rho u w \\ u(\rho E + p) \end{pmatrix} , \quad \vec{G} = \begin{pmatrix} \rho v \\ \rho u v \\ \rho v^2 + p \\ \rho v w \\ v(\rho E + p) \end{pmatrix} , \quad \vec{H} = \begin{pmatrix} \rho w \\ \rho u w \\ \rho v w \\ \rho w^2 + p \\ w(\rho E + p) \end{pmatrix} , \tag{4.4}$$

$$\vec{Q} = \begin{pmatrix} 0 \\ 0 \\ \Omega^2 y - 2\Omega w \\ \Omega^2 z + 2\Omega v \\ 0 \end{pmatrix} . \tag{4.5}$$

In these vectors, E is the total rotary internal energy given by

$$E = e + \frac{1}{2}\left(u^2 + v^2 + w^2\right) - \frac{1}{2}\Omega^2 r^2 . \tag{4.6}$$

In MTFLOW, the differential continuity and energy equations (the first and last equations respectively) are not actually solved. Instead a constant mass flow is prescribed along each streamtube to enforce continuity and the total enthaply is prescribed at every point in the flowfield to satisfy the energy equation. These parameters are then used as input to the streamwise momentum equation, which in MTFLOW has the form

$$dp + \rho q dq + \rho V_\theta dV_\theta + pd(\Delta S) - \rho d(\Delta W) = 0 \ . \tag{4.7}$$

With some manipulation, this can be converted to the entropy-convection equation

$$-pdS + pd(\Delta S) + \rho d(\Delta H) = 0 \ . \tag{4.8}$$

In MTFLOW either equation can be used, depending on the user's specified preference.

The geometric inputs required by MTFLOW include the flowpath and axial blade projections. For each blade row, the number of blades and non-dimensionalised wheel speed must also be specified. The blockage, circulation (rv), and adiabatic loss (ΔS) at each blade row are input as spanwise profiles. The output from MTFLOW includes the positions of streamlines, radial profiles of Mach numbers, flow angles, diffusion factors, and pressure ratios, and actual blade chord lengths (found from the computed flow angles and given axial chord lengths). The pressure contours are also computed.

Since some of the quantities computed by MTFLOW are variables that may be inputs to the design process — most importantly in this case the pressure ratios, chord lengths and stator exit flow angles — the results from MTFLOW will not necessarily agree with the initial design intent. The extent to which they do agree is highly dependent on the accuracy of the analysis with which the MTFLOW input values are obtained. Therefore, some iteration is usually required to obtain the desired values.

4.3.2 Results

The pressure contours from the throughflow solution are shown in Figure 4-4. The contours show a high static pressure rise across the second stage as compared to the first stage (due to the higher pressure in the second stage). A region of low static pressure rise can be seen near the hub of the first stage from rotor mid-chord to stator mid-chord, similar to that seen in Merchant's high-speed aspirated compressor [18]. This is due to the low reaction at the hub. This phenomenon is not seen in the second stage which has less spanwise variation in reaction.

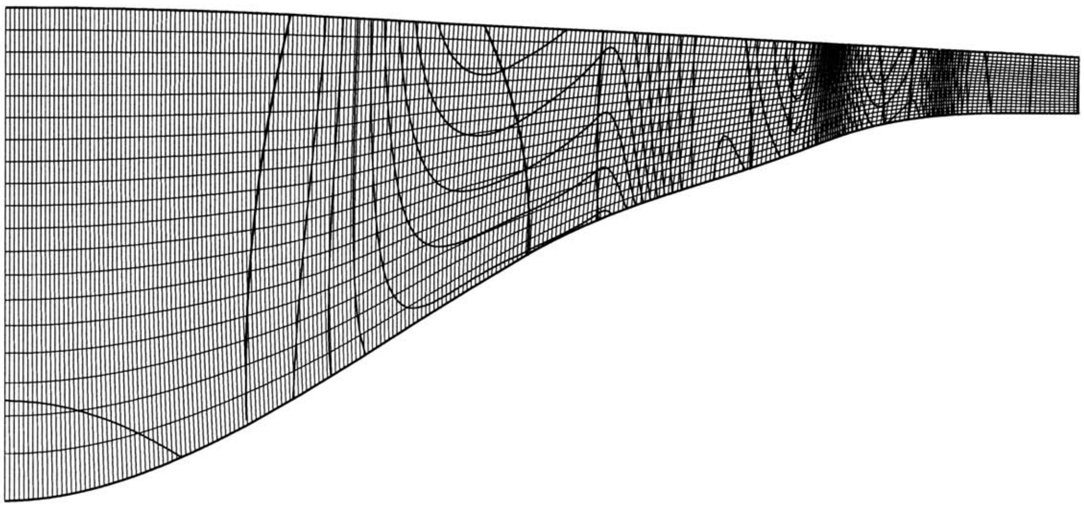

Figure 4-4: Throughflow pressure contours

4.4 Design Summary

The important parameters of the compressor design as determined from the stage analysis and throughflow computations are given in Table 4.1. The overall pressure ratio of the compressor is about 9.2:1 which is short of the initial goal of 10:1, but was the maximum determined to be feasible within the diffusion factor constraints. The pressure ratios and stage loading coefficients for each stage are noticeably higher than those expected for conventional core compressor stages. The reaction for the second stage is also relatively high indicating that the rotor shares a disproportionately high fraction of the loading. The velocity triangles at hub and tip for each blade row are shown in Figure 4-5.

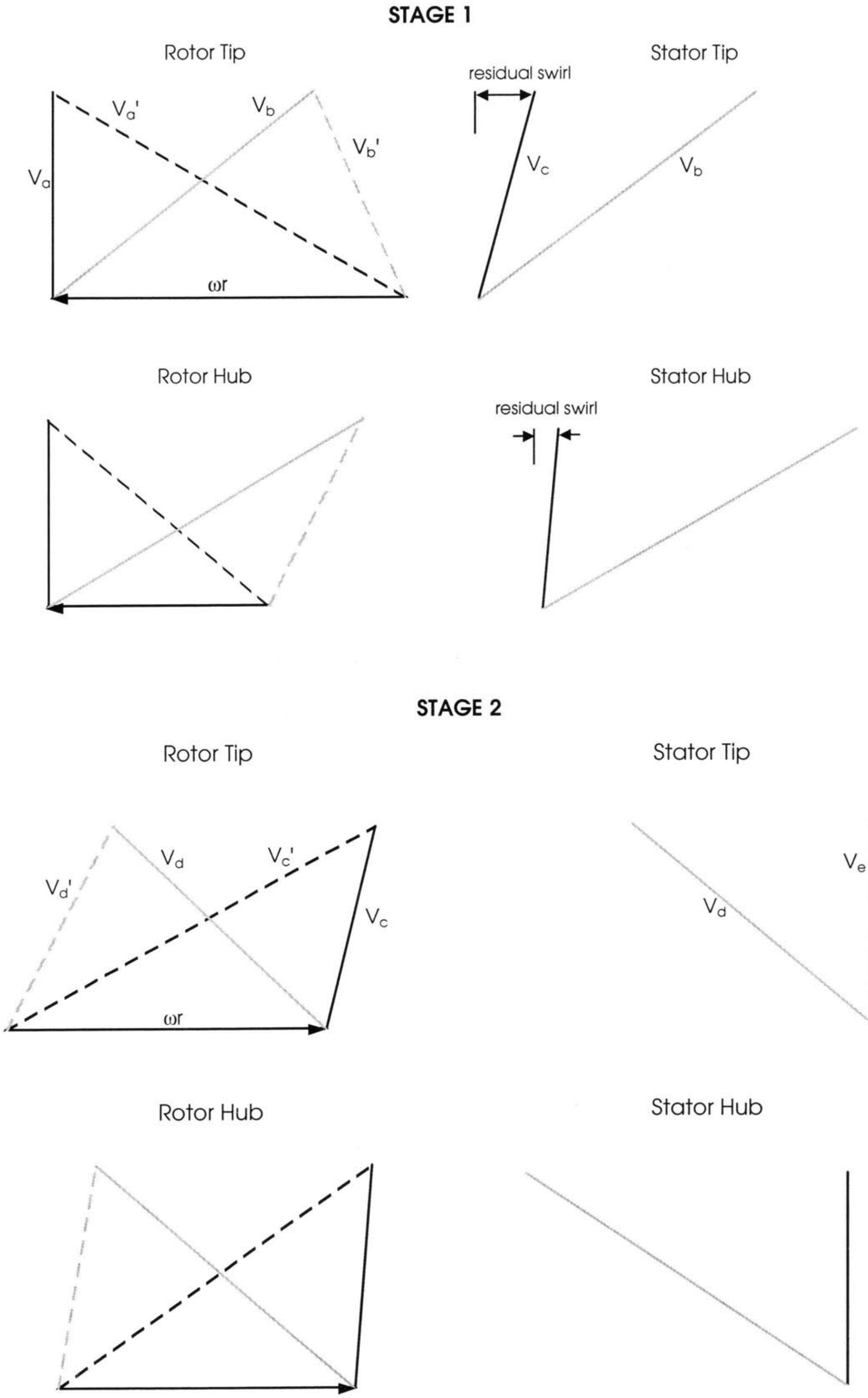

Figure 4-5: Velocity triangles

	Stage 1	Stage 2
Tip speed	457 m/sec	-457 m/sec
Rotor pressure ratio	3.60	2.75
Stage pressure ratio	3.40	2.70
Estimated (average) efficiency	93%	95%
Meanline reaction	0.58	0.72
Flow coefficient	0.58	0.5
Stage loading coefficient	0.70	0.77
Rotor hub solidity	3.5	3.5
Stator hub solidity	3.0	3.0
Inlet corrected mass flow	212 $kg/sec \cdot m^2$	
Inlet hub/tip radius ratio	0.5	
Outlet hub/tip radius ratio	0.92	
Length/inlet radius ratio	1.13	

Table 4.1: Stage design results

Chapter 5

Blade Design

The blade design process involved first designing two-dimensional sections and then stacking the sections radially to produce a three-dimensional blade shape. The blade sections were designed with a turbomachinery cascade code using data extracted from the throughflow solution. This included streamline radii, inlet and outlet flow conditions, chord length, and pitch. In the process of designing the blade sections, an attempt was made to reduce the complexity and difficulty of high-speed aspirated blade design by analysing the relationships between features of previously designed blades.

5.1 Code Description

The blade design code used was MISES, a quasi-three-dimensional turbomachinery cascade solver developed at MIT by Drela et al [7, 25]. In MISES, the flow field is divided into a viscous region, extending from the body surface to a height equal to the displacement thickness of the boundary layer, and an inviscid region outside of this. In the viscous region, the flow is modelled by a two-equation integral boundary layer formulation. In the inviscid region, the flow is governed by the 3-D Euler equations (given in Equations 4.2 to 4.5) projected onto an axisymmetric streamsurface of varying radius and thickness. As with MTFLOW, either the standard momentum equation (4.7) or the entropy convection equation (4.8) can be solved depending on the user's specification. The viscous and inviscid equations are coupled in MISES via the edge velocity and displacement thickness to yield a system of non-linear equations which are solved simultaneously.

In addition to blade analysis, MISES has inverse-design capabilities. Both mixed-inverse and modal-inverse methods are available, but the former was used in this work. In mixed-inverse design, the desired pressure distribution over a segment of the blade is prescribed by modifying the distribution for a seed geometry. MISES then perturbs the seed geometry at each point to achieve the specified pressure. The camber and thickness of the blade can be preserved during inverse design if desired.

The geometric inputs required for MISES include the blade coordinates and pitch and the radius and thickness of the stream surface on which the blade-to-blade flow is computed. The latter is provided by the throughflow code. The input flow conditions required depend on the boundary conditions imposed and can vary as the calculation proceeds. All of the relevant parameters, including the inlet and outlet Mach numbers, flow angles, and pressures are provided by the throughflow code. For the high-speed blades designed in this work, the boundary conditions generally imposed were the inlet Mach number and pressure, the so-called leading edge Kutta condition (for blades with non-sharp leading edges), the trailing edge Kutta condition and either the inlet flow slope or the exit pressure.

Given the above boundary conditions, the outputs from MISES include cascade exit quantities such as the Mach number, flow angle, and pressure. The viscous and shock losses and the diffusion factor for the blade section are also computed.

In the version of MISES used for this work, the boundary layer formulation includes a suction model. The required inputs to this model are the suction coefficient, c_m (given by equation 2.25), and the location and length of the suction slot. When suction is applied it decreases the boundary layer displacement thickness, so it appears as a negative displacement of the streamline at the edge of the viscous layer.

5.2 Design Process

The design process for a blade section is broken up into an inviscid design (represented in MISES by setting the Reynolds number equal to zero) and a viscous design. The steps followed to design the blades in this work are outlined as a flowchart in Figure 5-1.

The process begins with a seed geometry that is generally a previous design that has similar turning (defined as the difference between the exit and inlet flow angles) and inlet Mach number to the present design. A suitable inviscid design is then found by alternately modifying the geometry manually and using the inverse design capabilities of MISES. Often a slightly increased back pressure is imposed during this phase of the design to simulate the effects of viscosity, particularly the deviation of the flow at the blade trailing edge.

For the inviscid design, the geometry modification generally involves choosing the maximum camber to produce the required turning and setting the maximum thickness location based on the shock impingement point. The leading edge radius is chosen according to the inlet Mach number. The stagger angle required to achieve the desired incidence is also found. The choice of these parameters will be discussed in more detail in Section 5.3. The manual geometry modification is performed with XFOIL, an inviscid airfoil design and analysis program developed by Drela [4].

In the inverse design mode, the pressure distribution is modified to match a subsonic, transonic, or supersonic template depending on the inlet Mach number. The templates are shown in Figure 5-2 with the important features noted. Inverse design is particularly useful for smoothing the pressure distribution, eliminating pressure spikes at the leading edge where the flow transitions to the pressure and suction surfaces, and reducing the shock strength by adding precompression. Often the blade shape produced through inverse design has local kinks or bumps. This usually occurs when the pressure distribution is prescribed across a shock. These defects in the blade surface are smoothed manually using XFOIL.

Small bumps in the blade surface that are produced through inverse design or

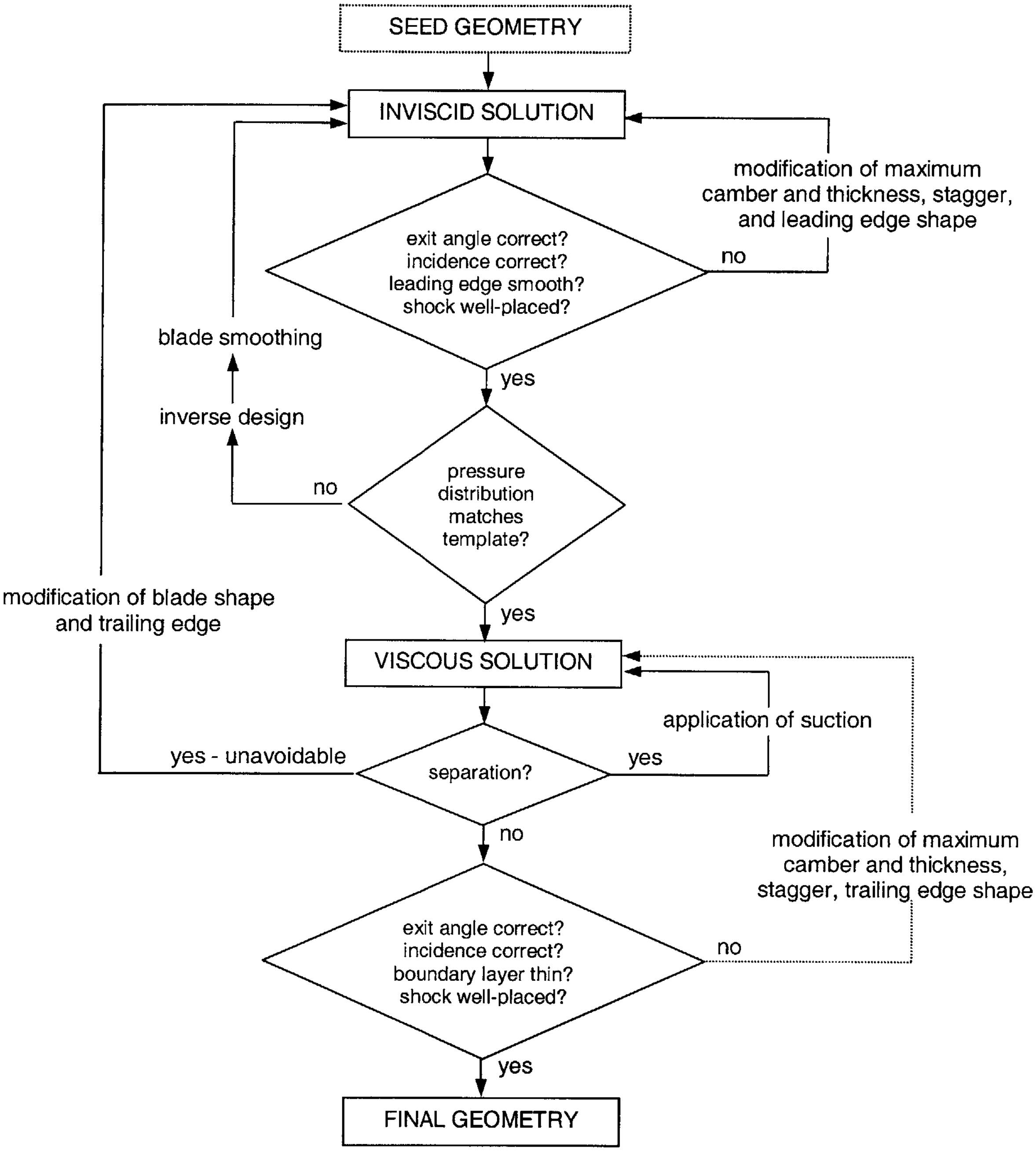

Figure 5-1: Blade section design flowchart

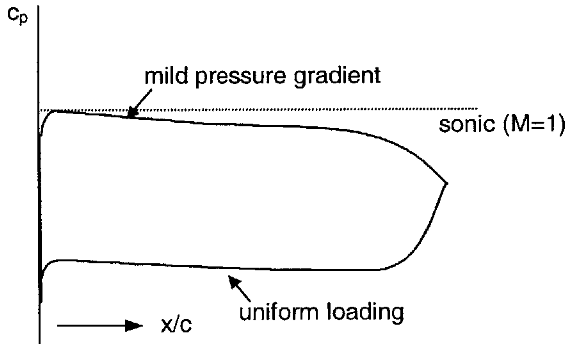

(a) Subsonic

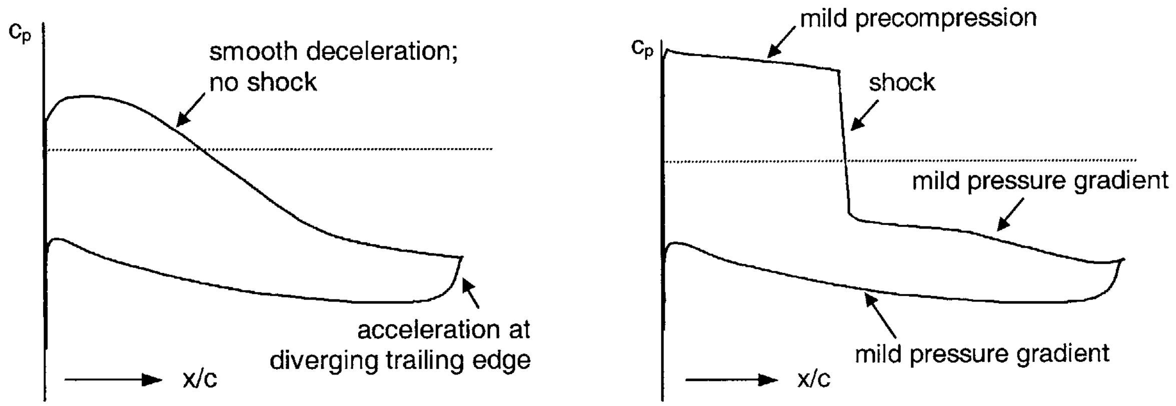

(b) Transonic

(c) Supersonic

Figure 5-2: Blade pressure distribution design templates otherwise can be difficult to detect visually, but will be detrimental to the off-design performance of the blade. The bumps can be located by computing the inviscid pressure distribution over the airfoil using the BLDSET function in MISES. The presence of a bump will result in a local peak in the pressure distribution. An example of a blade with a small bump is shown in Figure 5-3 with the corrected geometry overlayed. The corresponding inviscid pressure distributions are shown in Figure 5-4. The reduction in the pressure spike after the geometry modification can be clearly seen.

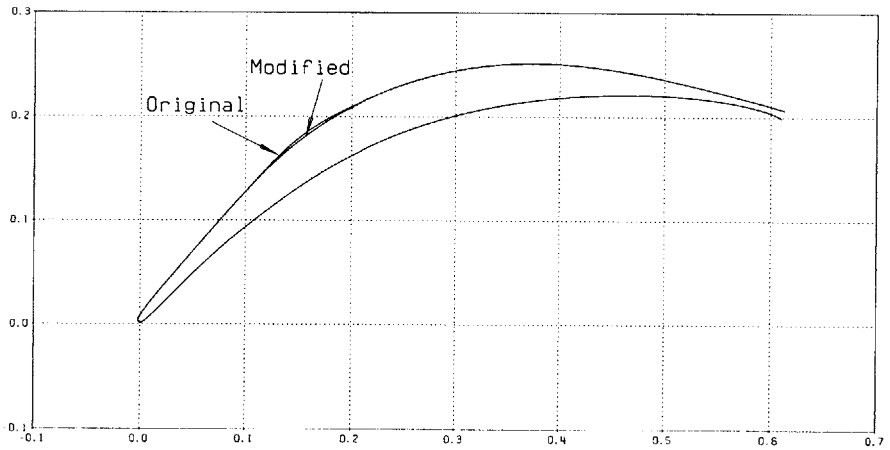

Figure 5-3: Correction of blade surface bump

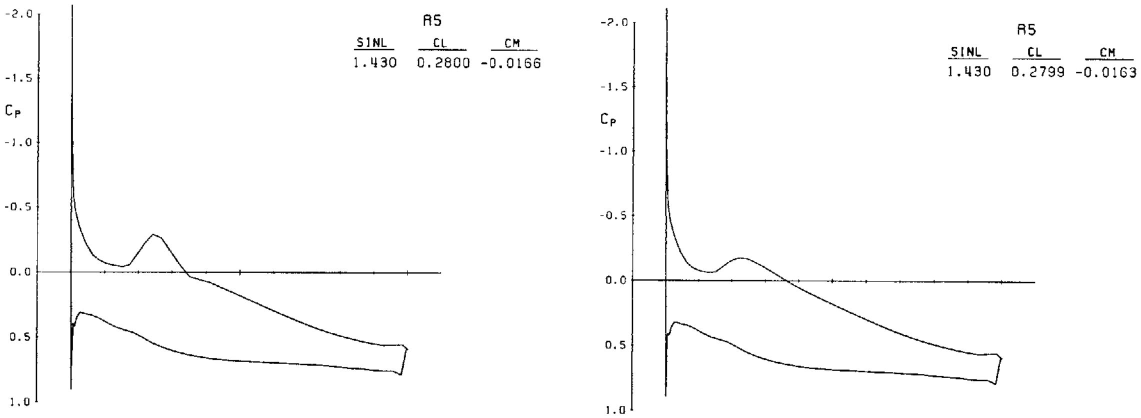

(a) Original blade with bump (b) Modified blade with reduced bump

Figure 5-4: Impact of blade surface bump on inviscid pressure distribution

Once an acceptable inviscid design for a blade section is obtained, the viscous solution is computed. The location of the suction slot and the amount of suction are chosen so as to prevent the boundary layer from separating. If the boundary layer is found to separate regardless of suction, the inviscid design must be modified. It is generally also necessary to slightly modify the maximum camber and thickness, incidence and trailing edge geometry in the viscous design phase. For supersonic blades, the inviscid solution must usually be re-converged after making geometry modifications and before proceeding with the viscous solution. Although inverse design can be used to modify the viscous design, it is not generally as effective as with the inviscid design, especially for supersonic blades. Inverse design cannot be used (convergence will not be reached) if the boundary layer is separated.

5.3 Blade Features

The main geometric and flow features of a high-speed aspirated compressor blade section are shown in Figure 5-5. Of the geometric variables labelled, only the blade spacing or pitch, p, inlet and outlet flow angles, β_1 and β_2, and chord length, c, are set in the stage design phase. The design of the blade section then involves fixing the other features: stagger angle, ξ, camber and thickness distributions, leading and

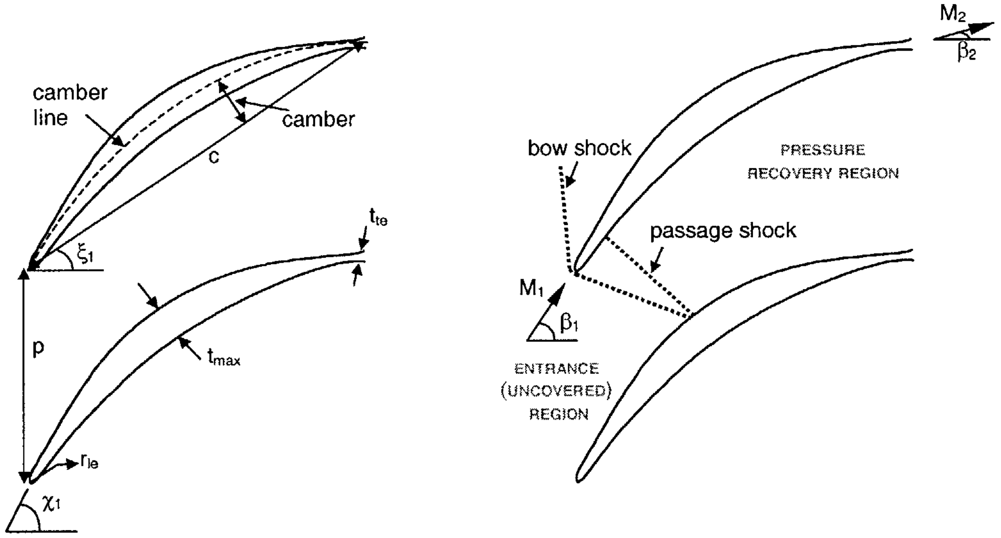

(a) Geometry parameters (b) Flow parameters

Figure 5-5: Blade section parameters

trailing edge geometries, and location and amount of aspiration.

Determining the optimum combination of these parameters to produce the required turning with minimum losses is not a straightforward process and depends heavily on the experience of the designer. As discussed in Section 5.2, the process is generally made easier (and quicker) by beginning with a previously designed blade with similar parameters to those sought. In this work, an attempt was made to reduce the subjectivity of the design process by identifying, and in some cases quantifying, the relationships between various parameters of high-speed aspirated blades. To this end, extensive analysis of the high-speed aspirated blade designs successfully completed by Merchant [18] was performed. These results were used to guide the initial design of some of the blades for the aspirated counter-rotating compressor, however a much larger design space was ultimately explored for the final designs. Therefore, data for these blades was included in the analysis to strengthen the results.

The following sections discuss the issues involved in designing a high-speed aspirated blade section with MISES. The focus is on the features that are directly modified in the design process. The relationships presented are useful for obtaining a good initial design for the blade although it is almost inevitable that some modification will be required to obtain the best possible final design. Merchant [18] provides a more detailed discussion of the theory behind the design of each region of the blade.

5.3.1 Incidence

The incidence of the blade is defined as the difference between the inlet flow direction and the projection of the blade camber line at the leading edge

$$i = \beta_1 - \chi_1 \ . \tag{5.1}$$

The angle of the blade camber line is in turn a function of the camber of the blade and the stagger, ξ, which is the angle of the chordline relative to the axial direction.

If the cascade passage is choked and the bow shock is attached to the leading edge of the blade, then the 'unique incidence' condition exists and the inlet flow angle is fixed for a given inlet Mach number, blade thickness, and blade suction surface angle. As described by Cumpsty [3], the 'unique incidence' inlet flow angle can be found from continuity and the Prandtl-Meyer relation applied along a characteristic extending from far upstream to the point, e, on the blade where the expansion wave from the leading edge of the adjacent blade intersects the suction surface,

$$\beta_1 + \nu(M_1) = \beta_e + \nu(M_e) \ . \tag{5.2}$$

To design blades with 'unique incidence' using MISES the cascade exit pressure is constrained and the leading edge geometry and stagger are chosen such that the calculated inlet flow angle matches that provided by the throughflow solution.

For most of the high-speed aspirated blades, the bow shock is actually slightly detached from the leading edge and some spillage of flow between cascade passages is possible. Therefore, the 'unique incidence' flow angle need not be matched exactly (it should be close, however, to keep mass flow capacity and efficiency high). There is also a computational advantage to constraining the inlet flow angle in MISES (to match the throughflow value) rather than the exit pressure and then choosing the leading edge geometry and stagger angle based on other criteria. In particular, it is desirable to minimize spikes in the pressure distribution on the suction and pressure sides of the blade at the leading edge and to reduce the leading edge shock loss (these properties are also affected by the leading edge geometry which will be discussed in Section 5.3.4). It was found in this work that using these criteria gives a blade design for which the 'unique incidence' flow angle matches the angle provided by the throughflow code very closely. This was confirmed by re-computing the flow over a completed blade without the inlet flow angle constrained.

With the leading edge geometry and camber angle fixed by other design considerations, the stagger angle is the primary variable used to obtain the correct incidence for the blade. For high-speed aspirated blades, the stagger angle that gives the correct incidence and the turning angle of the blade, $(\theta_2 - \theta_1)$, are highly correlated. Figure 5-6 shows the relationship. Once an approximate stagger angle is determined, it must generally be modified slightly throughout the design process as the geometry evolves.

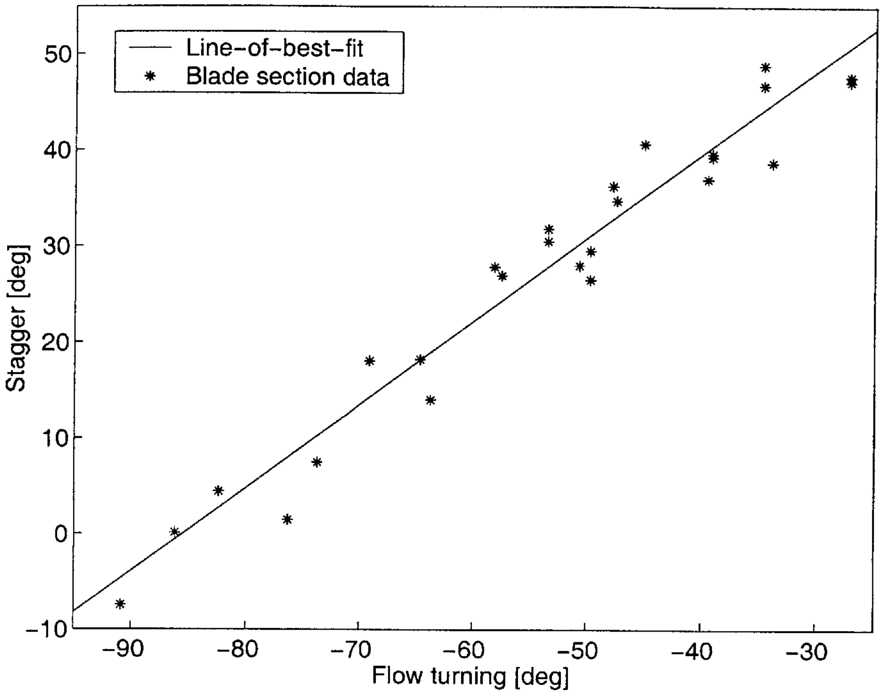

Figure 5-6: Stagger angle versus turning angle

5.3.2 Camber Distribution

The camber (or mean) line of a blade (shown in Figure 5-5(a)) is primarily shaped so as to provide the required flow turning. However, the optimum camber distribution also depends on such features as the blade stagger angle, desired pressure distribution, and deviation of the flow from the blade trailing edge due to viscous effects.

Although the exact shape of the camber distribution depends on several variables, the maximum value of the camber (normalized by the chord length) varies approximately linearly with the turning angle for high-speed aspirated blades. This is illustrated in Figure 5-7. Using this information an approximate value of the maximum camber for a blade can be set manually before proceeding with design of other features. Some modification of the camber is usually then necessary to achieve the correct exit angle, particularly once the extent of trailing edge deviation is known.

The maximum camber point is generally located just downstream of the shock impingement location, at the beginning of the pressure recovery region (shown in Figure 5-5(b)). Therefore, as the inlet Mach number increases and the shock impinges

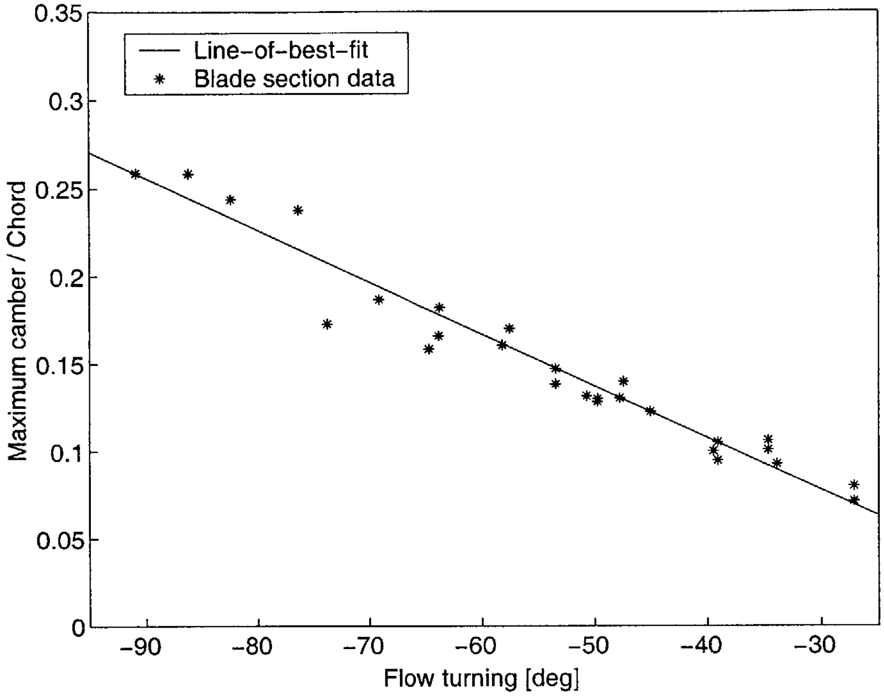

Figure 5-7: Maximum camber versus turning angle

further aft on the blade, the location of the maximum camber should also be moved back.

The distribution of camber forward and aft of the maximum depends largely on the desired pressure distribution and is therefore set through inverse design. In the entrance region (the uncovered region of the cascade passage as shown in Figure 5-5(b)), a slightly convex camber distribution is used for subsonic blades. For supersonic and supercritical blades, a flat or slightly concave distribution is used to achieve some compression of the flow so that the Mach number upstream of the shock, and hence the pressure loss through the shock, are reduced. However, as camber is removed from the entrance region it must be added to the rear portion of the blade to achieve the desired turning and this can lead to flow separation. Therefore, a balance must be reached between the benefit of precompression and the risk of downstream flow separation. For this reason, significant precompression is generally used only for sections near the tip of a blade where inlet Mach numbers and shock losses are particularly high and where the turning requirement is lower.

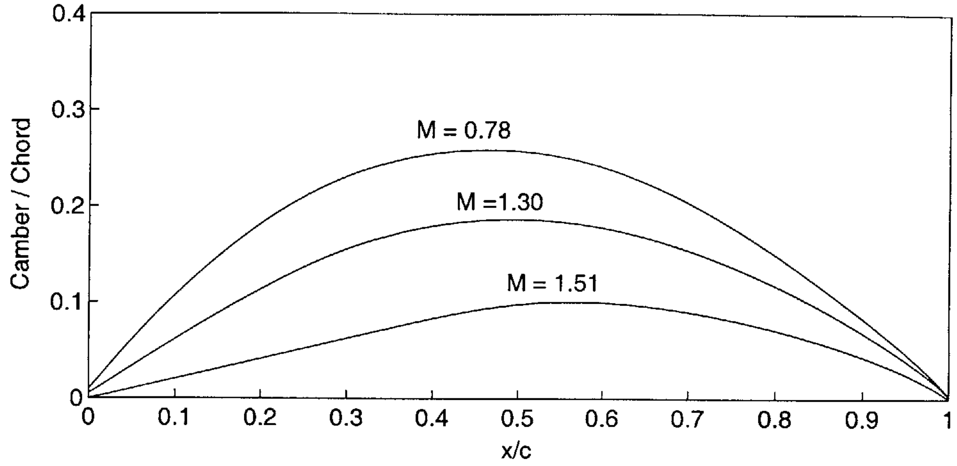

Figure 5-8: Typical rotor camber distributions

In the pressure recovery region of the blade, where the flow is subsonic, the camber distribution is shaped so as to evenly distribute the loading in the chordwise direction. If the boundary layer is found to separate readily, the camber is concentrated near the beginning of the pressure recovery region where the boundary layer is thinner and more capable of withstanding the increased loading. The camber at the trailing edge of the blade is determined by the choice of trailing edge features which are discussed in Section 5.3.5.

Some representative rotor camber lines are shown in Figure 5-8. The sections from which these camber lines come all belong to the same blade and therefore all have approximately the same pressure ratio. The variation with Mach number of maximum camber value and location and the different entrance region shapes can be seen.

5.3.3 Thickness Distribution

The thickness distribution of a blade section must satisfy both structural and aerodynamic constraints. The structural requirements limit the minimum thickness (or area) of the blade since it must be strong enough to withstand the forces exerted on it in operation, particularly the large radial forces. For this reason, the cross-sectional area of a blade is generally decreased with increasing radius (measured outward from the hub) so that the sections near the hub are able to support those near the tip. For constant-chord blades (such as those considered here), this means that the thickness is decreased with radius. The suction passage requirements also limit the minimum thickness of aspirated blades. Currently this requirement can only be estimated based on the low-speed aspirated stage that has been built and tested [21].

For satisfactory aerodynamic performance, the maximum thickness of the blade, which governs the size of the throat in the cascade passage, must be small enough to ensure that the required mass flow can be passed through the blade row. The approximate throat area needed, A_t, can be determined from the area ratio required for 'started' supersonic flow, A_t/A_i , where A_i is the cascade inlet area. For two-dimensional flow this is calculated from the pressure change across the shock (neglecting the effect of the boundary layer thickness). The throat area is also affected by the choice of solidity and stagger.

For high-speed aspirated blades, the areas of the sections are decreased approximately linearly with increasing radius while taking into account the constraints on maximum and minimum thicknesses described above, particularly the ability to pass the design mass flow. The maximum thicknesses for several sections of three high-speed aspirated blade rows (two rotors and a stator) are plotted in Figure 5-9 to show the typical values.

The location of maximum thickness is critical to the aerodynamic performance of the blade section since it influences where the cascade passage shock (shown in Figure 5-5(b)) is located. At the design point, the passage shock and bow shock should coalesce so that the boundary layer does not have to withstand two shock impingement points and the length of the subsonic pressure recovery region of the blade is maximised. This condition is achieved by placing the maximum thickness point just upstream of the bow shock impingement location. If the maximum thickness is aft of this point then the passage shock will move downstream. On the other hand, if the maximum thickness is forward of this point, the throat area will be decreased and the cascade may not pass the desired mass flow.

Away from the leading and trailing edges and the maximum thickness location,

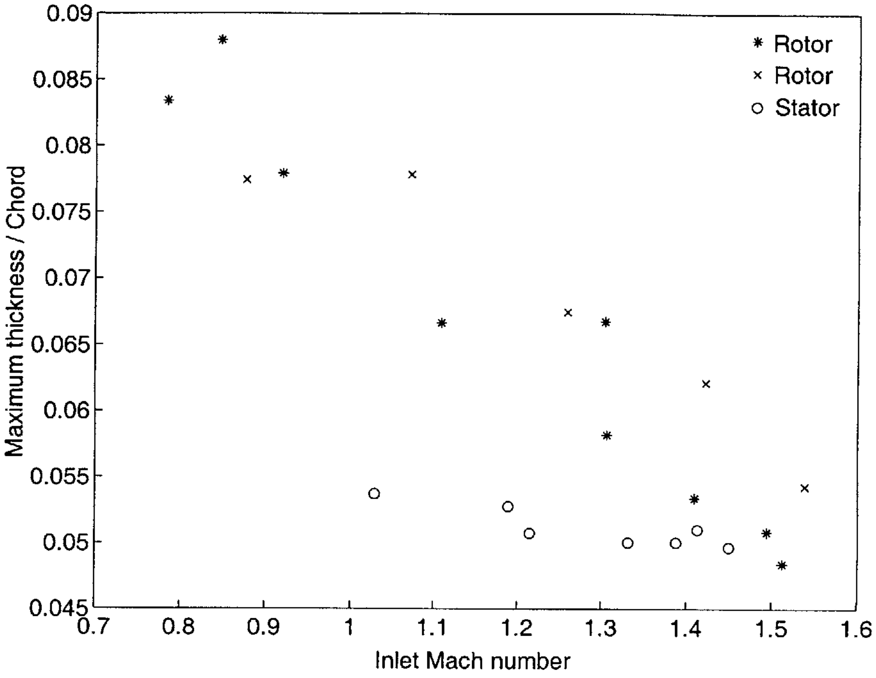

Figure 5-9: Maximum thickness versus inlet Mach number

the thickness distribution is set primarily through inverse design. Occasionally, the thickness in the pressure recovery region of the blade must be modified manually to prevent boundary layer separation.

5.3.4 Leading Edge

The goals in designing the leading edge of the blade are to minimise local losses and avoid spikes in the pressure distribution which can be detrimental to the downstream development of the boundary layer. The design is performed in parallel with the choice of stagger angle and camber distribution as discussed in Sections 5.3.1 and 5.3.2 respectively. The critical features of the leading edge are the radius or thickness and the blending with the pressure and suction surfaces.

The loss due to the leading edge thickness, t_{le}, has been shown to scale with $t_{le}M_1^2$ [13]. Therefore, as the inlet Mach number increases, the leading edge thickness should be decreased to keep losses low. There is, however, a limitation on the minimum leading edge thickness due to structural and manufacturing constraints, so

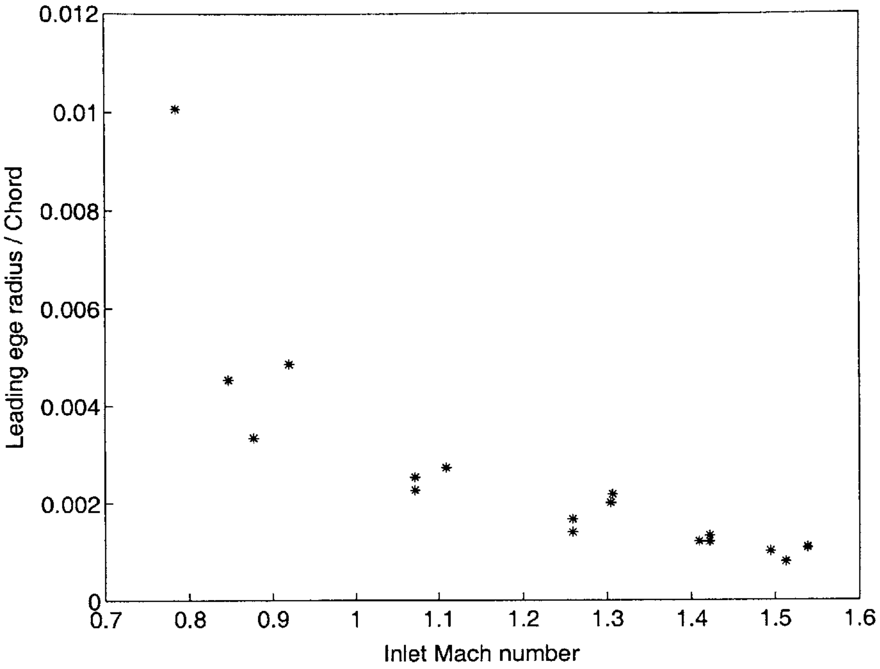

Figure 5-10: Leading edge radius versus inlet Mach number

above a certain Mach number the leading edge radii are approximately constant. For the high-speed aspirated blades the minimum radius used is about $0.002c$ (where c is the chord length). This trend is seen in Figure 5-10 which shows the leading edge radii for several high-speed aspirated blade sections versus the inlet Mach number.

The best blending of the leading edge with the pressure and suction surfaces is achieved through inverse design by imposing a pressure distribution with a smooth transition from the stagnation point to each side. Very pronounced blending is avoided as it can adversely affect the off-design performance of the blade. Occasionally manual modification is required to correct this problem.

5.3.5 Trailing Edge

The blades used in this compressor feature diverging trailing edges which are characterised by a finite thickness and divergence of the pressure surface from the suction surface as shown in Figure 5-11(a). The effect of the diverging pressure surface is to increase the pressure coefficient at the trailing edge, thereby increasing the loading, as shown in Figure 5-11(b). Drela and Schafer [6] provide a more detailed discussion of diverging trailing edges.

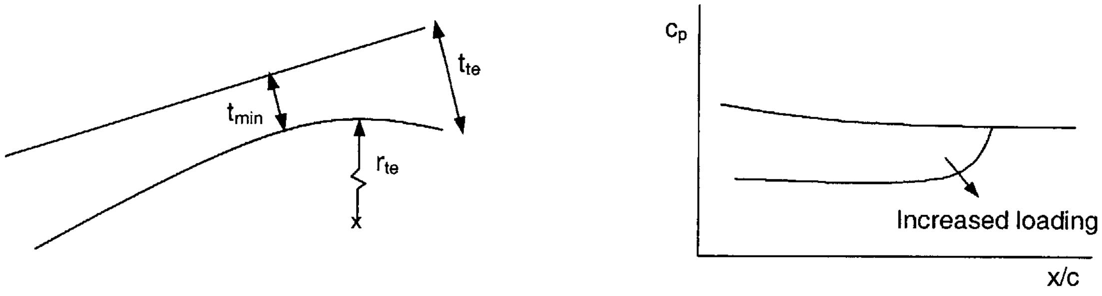

(a) Geometry

(b) Pressure distribution

Figure 5-11: Diverging trailing edge

By considering the pressure gradient due to curvature in the normal momentum equation it can be shown that the increase in loading at the trailing edge due to the divergence scales with the square of the difference between the trailing edge and minimum thicknesses, $(t_{te} - t_{min})^2$ [18]. Therefore it is desirable to maximize this difference within the structural and aerodynamic constraints on the blade.

The trailing edge thickness and shape are selected primarily so as to ensure that the boundary layer remains attached over the entire blade surface. The minimum thickness and its location are then chosen to maximise loading within the structural limitations. It is occasionally necessary to limit the amount of curvature on the pressure side to avoid boundary layer separation due to the adverse pressure gradient.

5.3.6 Aspiration

The important features of the aspiration that must be quantified when designing a blade section are the amount of suction (as a fraction of the inlet flow) and the location and length of the suction slot.

The location of the suction slot is chosen after the shock impingement location on the blade surface is known approximately. As discussed in Section 2.4, the slot should be placed just downstream of the impingement point. The amount of suction is then chosen so that it is sufficient to keep the downstream boundary layer attached. The suction coefficients required for high-speed aspirated blades have varied from about 0.5 percent to a maximum of about 2 percent (required at the tip sections of the rotor blades). Often some iteration between the location and amount of suction is required since the suction can cause the shock impingement location to move slightly.

When choosing the location and amount of suction it is useful to consider the development along the blade surface of the boundary layer shape parameter given by

$$H = \frac{\delta^*}{\theta} \tag{5.3}$$

where δ^* is the boundary layer thickness and θ is the momentum thickness. The shape parameter is computed by MISES and gives an indication of how close the boundary layer is to separation at each point. As a general rule it is desirable to keep the shape parameter well below 4 for laminar flow and 3 for turbulent flow.

For all of the high-speed aspirated blades designed to-date, a suction slot length of $0.02c$ (where c is the blade section chord length) has been used. This was found to be optimal on the basis of Merchant's work [18].

5.4 Final Blade Designs

The hub, 50% span, and tip section designs for each blade row are presented in the following sections. For each section the blade shape, surface isentropic Mach number distribution, and pressure contours are shown. The shape parameter distributions for two sections are shown to illustrate the effect of aspiration on boundary layer growth. 25% and 75% span sections were also designed for each blade row. The plots for these sections are included in Appendix A.

5.4.1 Stage 1

Rotor Hub

The Mach number distribution and pressure contours for the rotor hub section of the first stage are shown in Figure 5-12. The total pressure ratio of this section is 3.56. This is lower than the throughflow value of 3.6, but it was not possible to increase the turning any further without flow separation occurring (even with suction). The particularly high turning requirement is due the low radius and correspondingly low rotational speed at the hub.

On the suction surface of the blade section, the subsonic inlet Mach number accelerates to a slightly supersonic value, which it maintains for about 30% of the chord, and then gradually decelerates. The pressure contours show that the flow remains shock-free over the entire blade which helps keep the losses low. The pressure side has a mild adverse pressure gradient up to the trailing edge where the diverging surface causes a large acceleration.

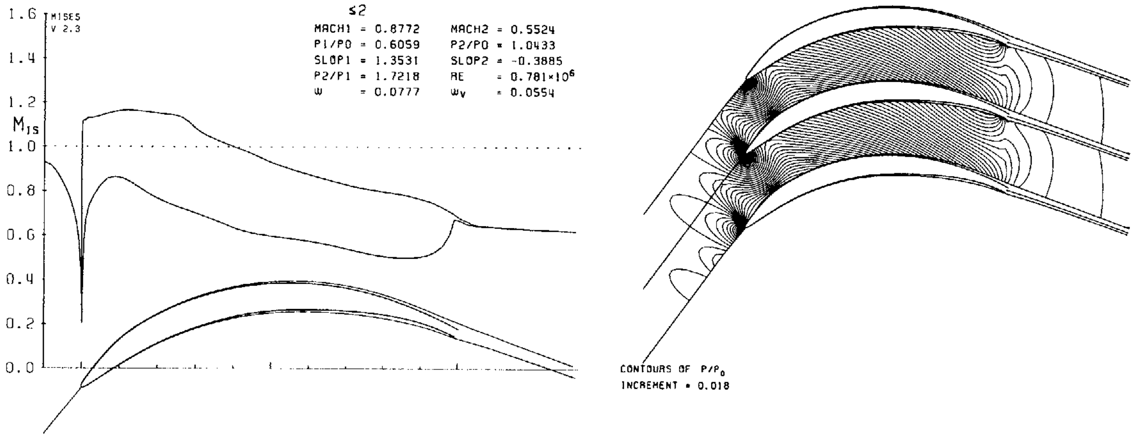

(a) Blade shape & Mach number (b) Pressure contours

Figure 5-12: Rotor 1 hub

Rotor 50% Span

The Mach number distribution and pressure contours for the 50% span blade section are shown in Figure 5-13. The total pressure ratio of this section is 3.58 which is close to the throughflow value. At this radius the inlet Mach number is supersonic and a strong shock is present. The location of the maximum thickness is such that the bow shock and passage shock coalesce as seen in the pressure contour plot. The camber distribution is shaped so as to provide a very small amount of compression upstream of the shock. Downstream of the shock, the loading on the suction surface is almost constant. On the pressure side there is an adverse pressure gradient up to about 30% chord after which there is constant loading until the diverging trailing edge.

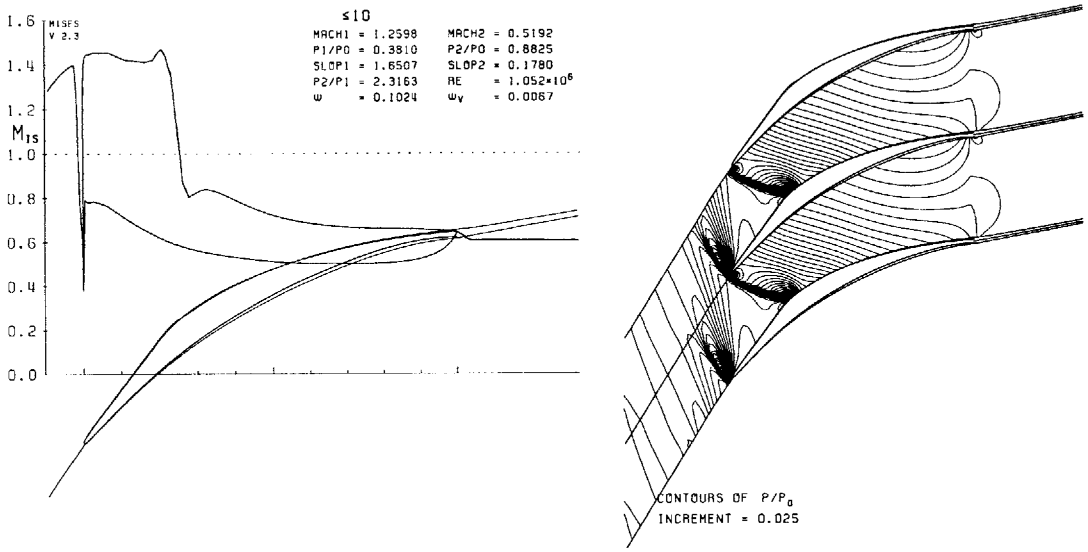

(a) Blade shape & Mach number (b) Pressure contours

Figure 5-13: Rotor 1 50% span

The shape parameter distribution for the 50% span rotor blade section is shown in Figure 5-14. The rapid increase in the shape parameter across the shock on the suction surface can be seen. As discussed in Section 5.3.6, suction is applied just downstream of the shock impingement point and reduces the shape parameter. Downstream of the suction slot the shape parameter remains almost constant at about 1.5 which is well below the limit of 3 or 4.

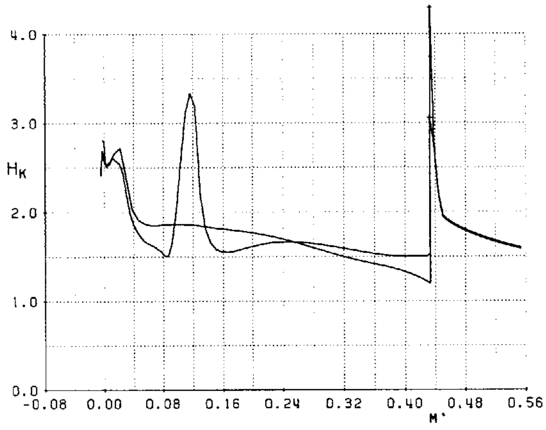

Figure 5-14: Rotor 1 50% span shape parameter

Rotor Tip

Figure 5-15 shows the Mach number distribution and pressure contours for the tip section of the first rotor. The total pressure ratio of this section is 3.58. The diffusion factor is 0.76 which is the highest value in the entire compressor. The section is characterised by a very high inlet Mach number and low turning requirement. The pressure contours show that the bow and passage shocks coalesce as desired. Significant precompression is applied upstream of the shock impingement point to keep the loss as low as possible. Even with this feature the shock loss accounts for over 95% of the total loss. Downstream of the shock the loading is constant over the suction surface. The loading is also constant over the entire pressure surface with a very small acceleration at the trailing edge. In this case the effectiveness of the diverging trailing edge is reduced because of the thick boundary layer. The suction requirement for this section is 2.1% (of the inlet mass flow) which is the highest requirement in the compressor.

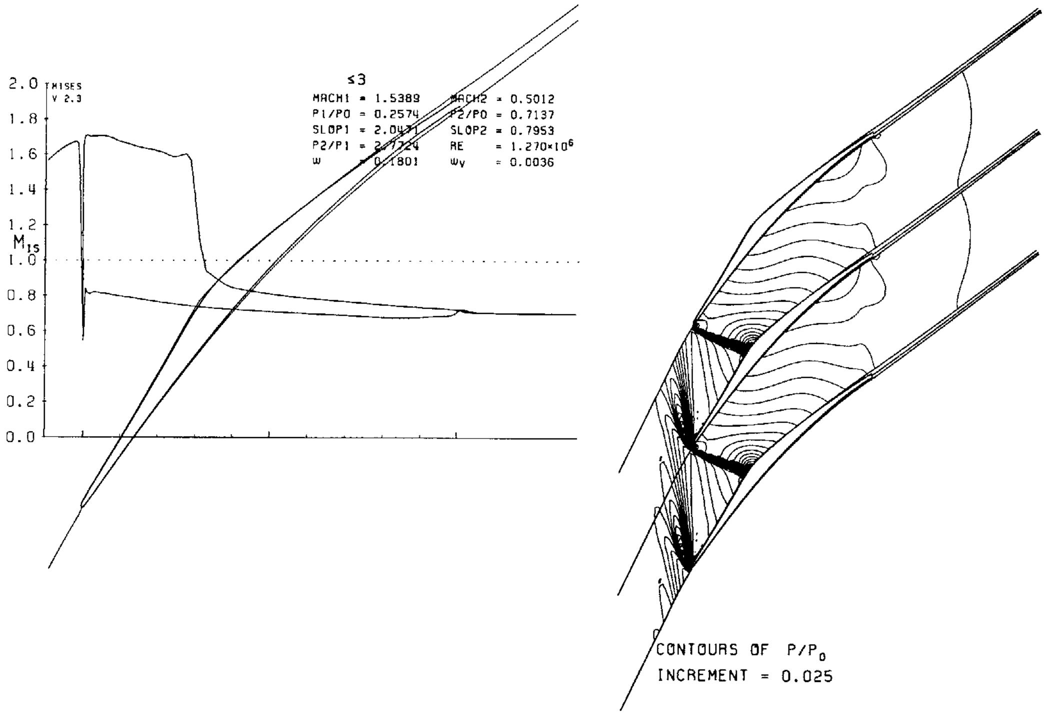

(a) Blade shape & Mach number (b) Pressure contours

Figure 5-15: Rotor 1 tip

Stator Hub

The Mach number distribution and pressure contours for the hub section of the first stator are shown in Figure 5-16. The pressure ratio is 0.95. The turning requirements for each section in this blade row are approximately the same due to the choice of exit angle distribution. Therefore, the blade shapes are very similar except for the differences necessitated by the varying inlet Mach number.

On the suction side of the hub blade section there is some precompression upstream of the shock followed by a very mild deceleration downstream of the shock. The pressure side has a mild adverse pressure gradient up to the diverging trailing edge where the flow accelerates.

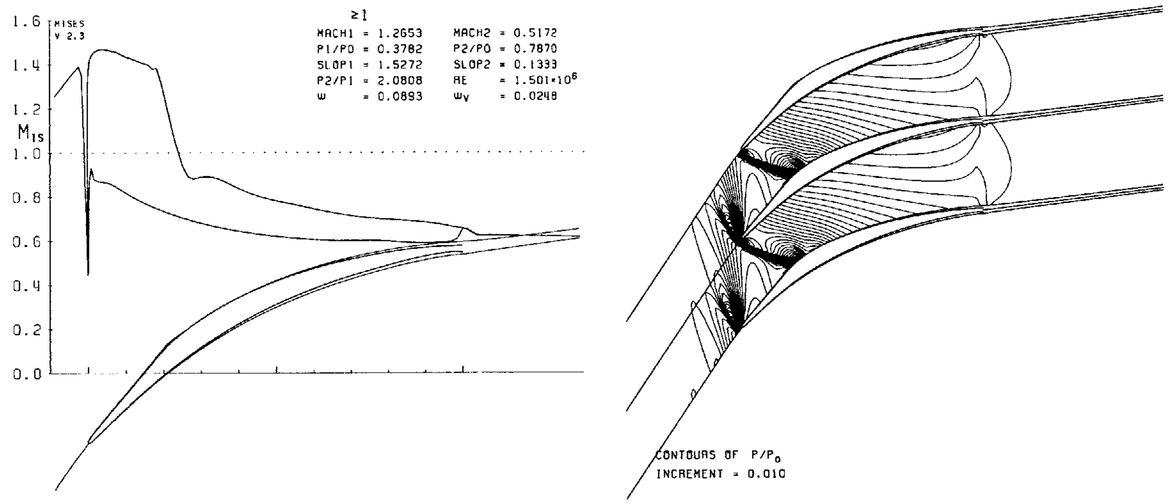

(a) Blade shape & Mach number (b) Pressure contours

Figure 5-16: Stator 1 hub

Stator 50% Span

Figure 5-17 shows the Mach number distribution and pressure contours for the 50% span section of the first stator. The pressure ratio is 0.97. This section is very similar to the hub section except for the lower supersonic inlet Mach number and correspondingly milder precompression. The shock loss is noticeably lower than for the hub section.

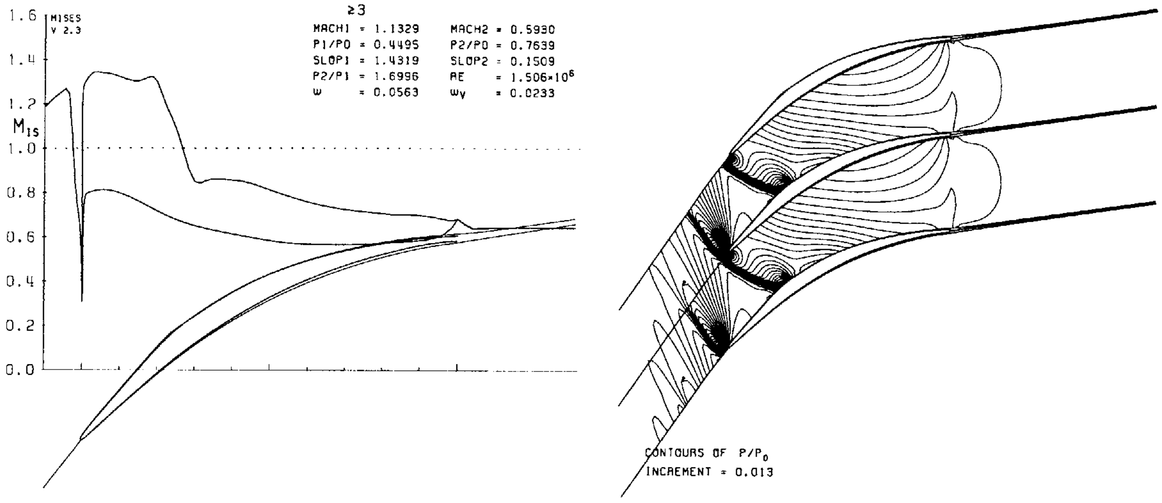

(a) Blade shape & Mach number

(b) Pressure contours

Figure 5-17: Stator 1 50% span

The shape parameter distribution for the 50% span stator blade section is shown in Figure 5-18. The increase in the shape parameter across the shock is much lower than for the rotor 50% span section due to the lower inlet Mach number and weaker shock. As a result the amount of suction required to keep the shape parameter below 4 and control the boundary layer is lower. Downstream of the suction slot the shape parameter remains approximately constant as for the rotor section.

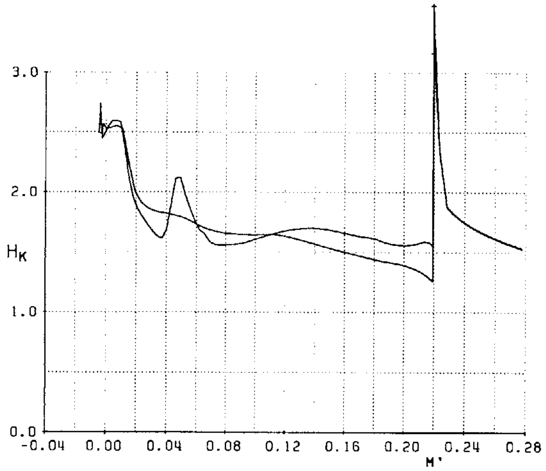

Figure 5-18: Stator 1 50% span shape parameter

Stator Tip

Figure 5-19 shows the Mach number distribution and pressure contours for the stator tip section. The pressure ratio is 0.98. The large Mach number drop across the tip of the first rotor results in a sonic inlet Mach number at the stator tip. This causes the diffusion factor and suction requirement at the tip to be the lowest in the blade row. The low Mach number also causes the bow shock to be completely detached from the leading edge and to impinge relatively far forward on the adjacent blade as seen in the pressure contour plot. Downstream of the shock impingement point, there is a mild deceleration over the suction surface. On the pressure surface there is a very mild deceleration up to about 50% chord and then approximately constant loading up to the trailing edge.

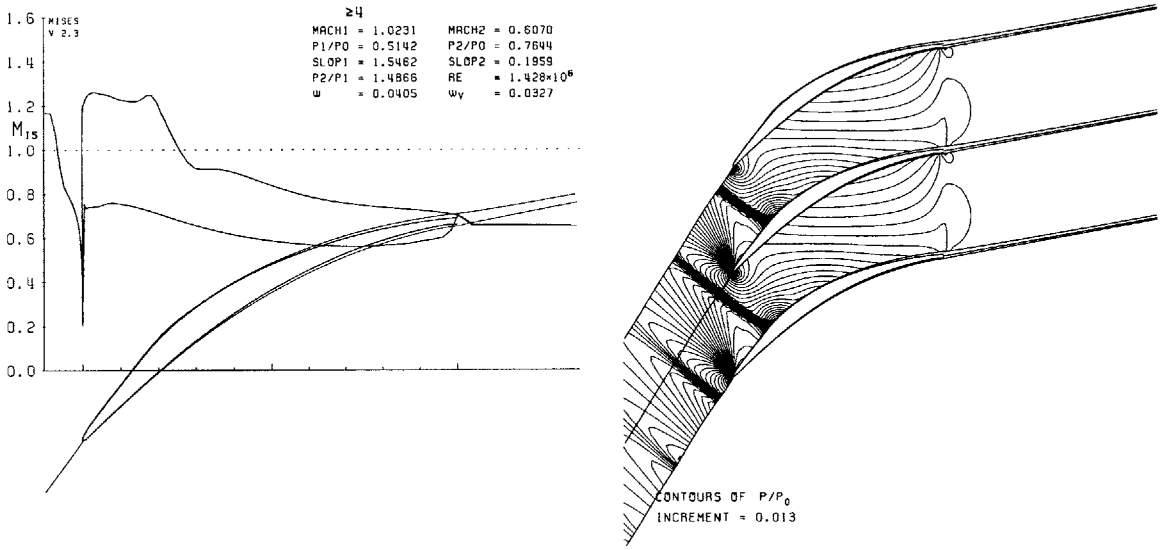

(a) Blade shape & Mach number (b) Pressure contours

Figure 5-19: Stator 1 tip

5.4.2 Stage 2

Rotor Hub

Some modifications of the stage design parameters for the second rotor were required when designing the blade sections with MISES. Most notably the hub solidity was reduced from 3.5 to 2.0 because it was found that in the tip region the blade row could not pass the design mass flow. Relatively low stagger angles were also used to increase the cascade passage throat area.

The Mach number distribution and pressure contours for the hub section of the second rotor with decreased solidity are shown in Figure 5-20. The total pressure ratio of the section is 2.68. The diffusion factor is 0.71 which is the highest value for the blade row. This differs from conventional rotors for which the highest diffusion factor typically occurs at the tip. The inlet Mach number of 1.2 is also relatively high for a rotor hub due to the residual swirl left in the flow from the first stage. This results in a strong shock and correspondingly high loss. Downstream of the shock the deceleration is very mild to prevent flow separation. This is also the case on the pressure side of the blade.

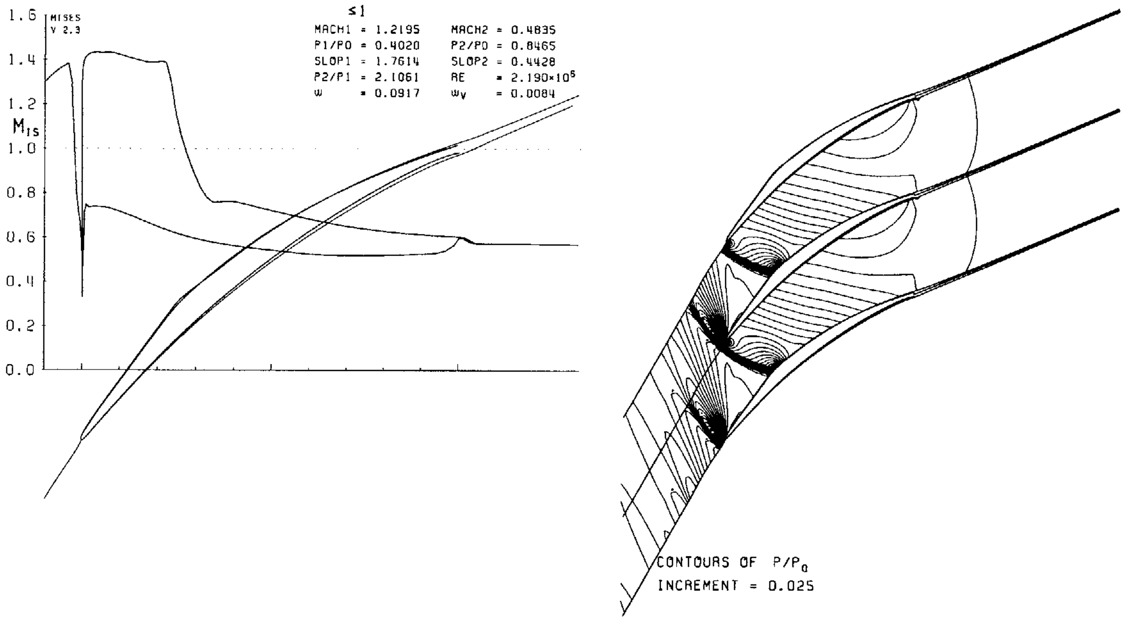

(a) Blade shape & Mach number (b) Pressure contours

Figure 5-20: Rotor 2 hub

Rotor 50% Span

Figure 5-21 shows the Mach number distribution and pressure contours for the 50% span section of the second rotor. The pressure ratio of the section is 2.58. Due to the high inlet Mach number, this section has some precompression to keep shock losses low. Almost all of the deceleration of the flow on the suction side takes place across the shock and the downstream Mach number is approximately constant. Likewise, on the pressure side, the Mach number is almost constant except for a spike near the leading edge. The spike is the result of the low stagger angle used to increase the cascade passage throat area and lower the suction surface inlet Mach number.

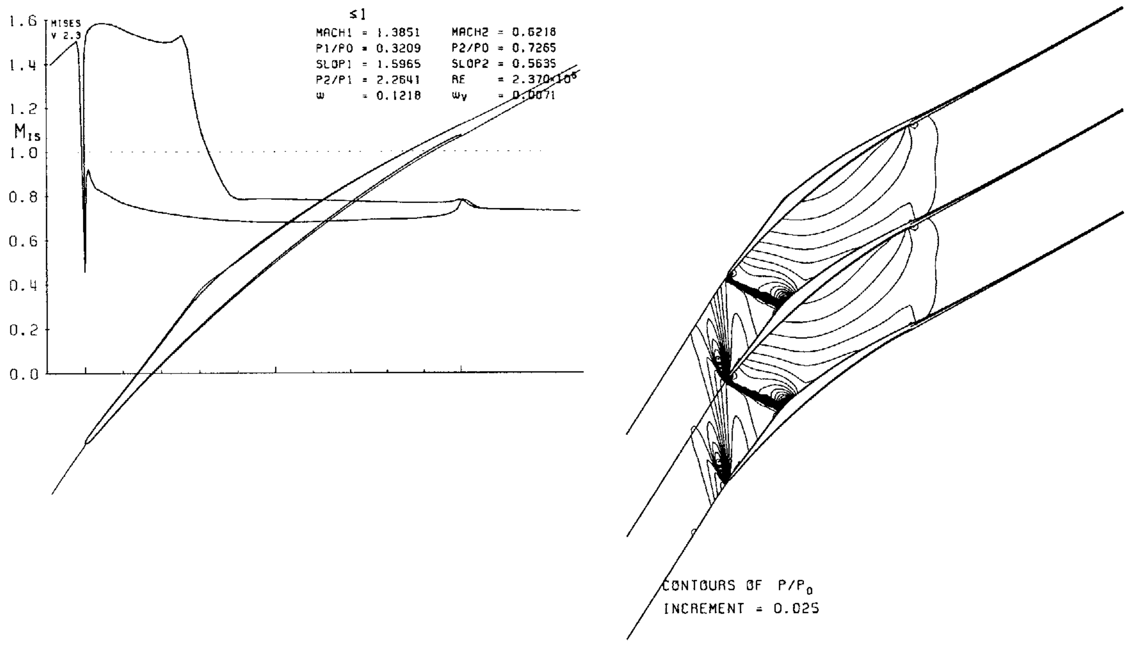

(a) Blade shape & Mach number (b) Pressure contours

Figure 5-21: Rotor 2 50% span

Rotor Tip

For the tip and 75% span sections of the second rotor, converged viscous solutions could not be obtained with MISES. Therefore, the designs were completed based solely on the inviscid analysis. It was concluded that the problems were likely computational in nature and that the 3-D analysis could be used to determine the viscous effects on the blade section performance.

The inviscid Mach number distribution and pressure contours from MISES for the tip section are shown in Figure 5-22. The corresponding pressure ratio is 2.65. This section has significant precompression to lower the peak Mach number of almost 1.8 to about 1.5 just upstream of the shock. Downstream of the shock, there is a very mild deceleration. On the pressure side, there is a small spike at the leading edge as there is for the 50% span section.

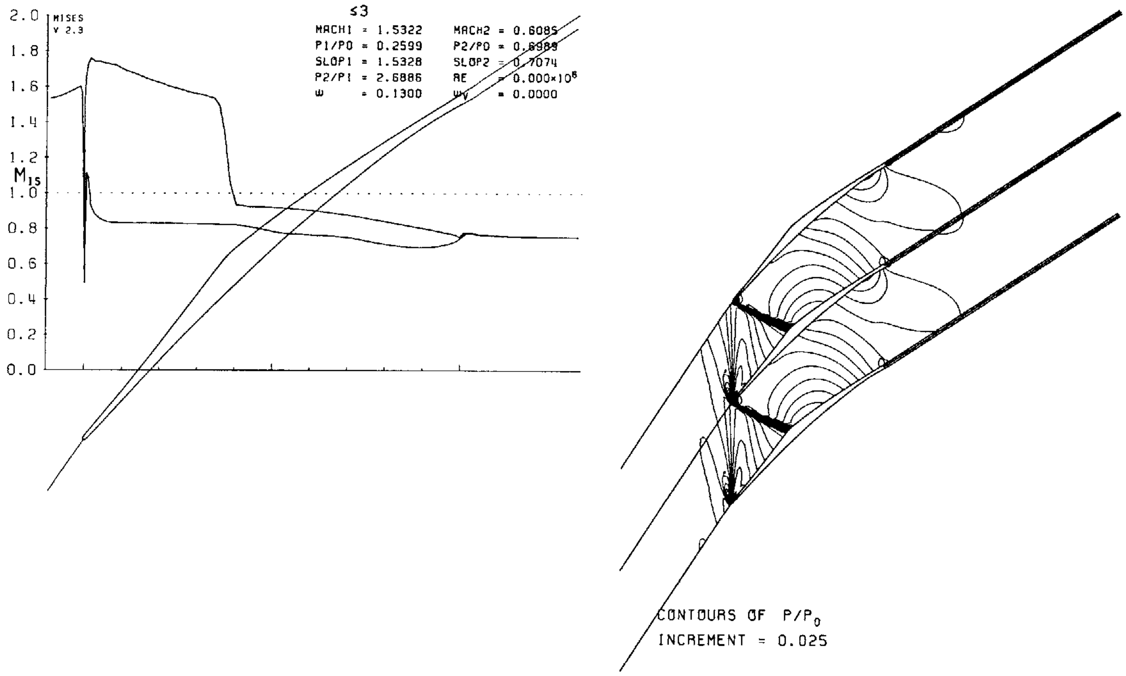

(a) Blade shape & Mach number

(b) Pressure contours

Figure 5-22: Rotor 2 tip

Stator Hub

The Mach number distribution and pressure contours for the hub section of the second stator are shown in Figure 5-23. The pressure ratio is 0.99. Unlike the other blade rows, this stator has subsonic inlet Mach numbers along the entire span so the sections are characterised by large thicknesses and leading edge radii. For the hub section, only a small region of the flow near the leading edge of the suction surface is slightly supersonic. Downstream of this region, the Mach number decelerates up to mid-chord. The pressure contours show that the flow remains shock-free. Due to the high turning requirement for this section (and the other sections in the stator), suction is required to keep the boundary layer attached. This causes the sharp drop seen in the Mach number distribution near mid-chord. On the suction surface there is a relatively rapid deceleration up to mid-chord and then constant loading up to the trailing edge. The effect of the diverging trailing edge is small because of the thick boundary layer.

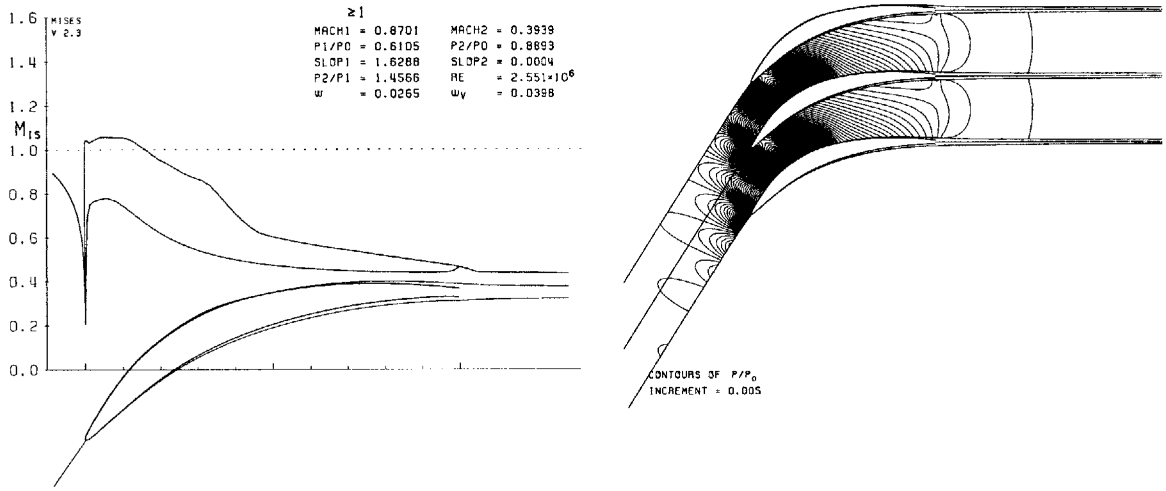

(a) Blade shape & Mach number (b) Pressure contours

Figure 5-23: Stator 2 hub

Stator 50% Span

Figure 5-24 shows the Mach number distribution and pressure contours for the 50% span section of the second stator. The pressure ratio is 0.99. This section is very similar to the hub section except that the suction is applied further downstream. The deceleration of the flow on the pressure surface is also more gradual and extends over almost the entire length of the blade.

Stator Tip

Figure 5-25 shows the Mach number distribution and pressure contours for the tip section of the stator. The pressure ratio is 0.99. This section is again very similar to the hub and 50% span sections. However, for this section, the region of supersonic flow extends almost to mid-chord at which point the suction is applied. The Mach

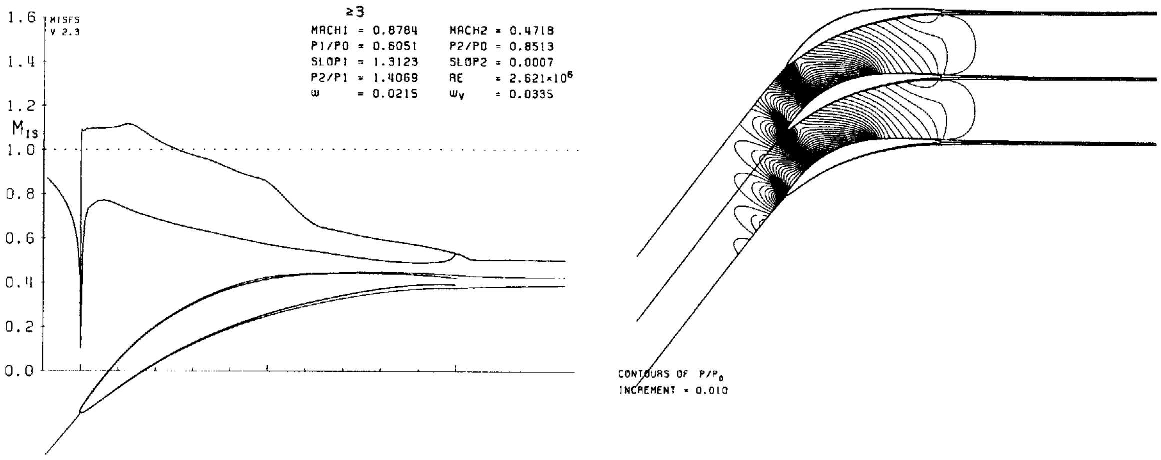

(a) Blade shape & Mach number (b) Pressure contours

Figure 5-24: Stator 2 50% span

number distribution on the pressure side is almost identical to that for the 50% span section.

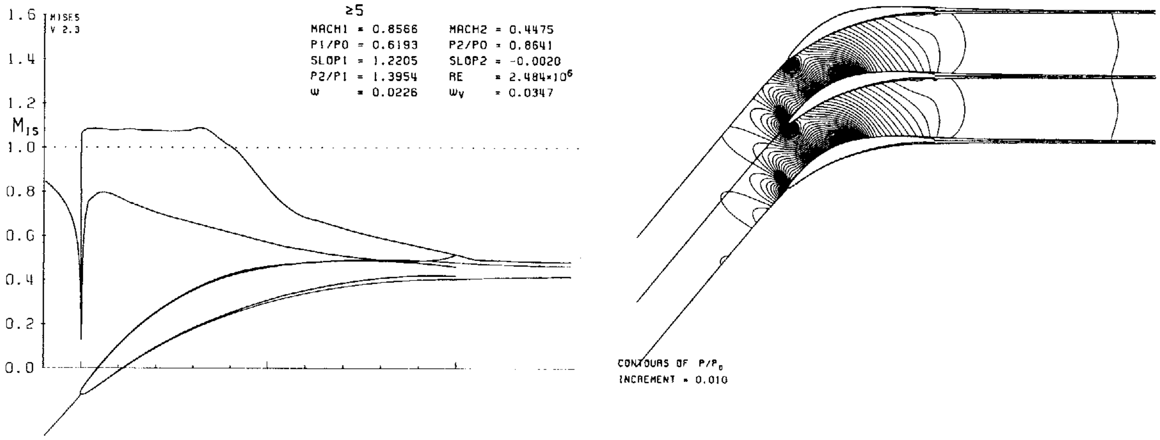

(a) Blade shape & Mach number (b) Pressure contours

Figure 5-25: Stator 2 tip

5.4.3 Summary

The properties of the stages based on the MISES blade section designs are summarised in Table 5.1. The pressure ratios and efficiencies are given as spanwise averages (over the five sections designed for each blade row). The properties for the second rotor include the values for the tip sections which are based only on inviscid analyses. The suction requirements are based on the maximum requirement in the blade row and are given as a percentage of the inlet mass flow.

	Stage 1	Stage 2
Rotor pressure ratio	3.59	2.67
Stage pressure ratio	3.46	2.64
Rotor isentropic efficiency	94.0 %	91.8 %
Stage isentropic efficiency	93.5 %	91.4 %
Maximum rotor diffusion factor	0.76 (tip)	0.71 (hub)
Maximum stator diffusion factor	0.67 (hub)	0.67 (hub)
Rotor suction requirement	2.1 %	2.0 %
Stator suction requirement	1.3 %	1.5 %

Table 5.1: MISES design results

Chapter 6

Conclusion

A quasi-three-dimensional, MISES-based design of a two-stage aspirated counter-rotating compressor has been completed. The combination of aspiration and counter-rotation enables both stages to produce pressure ratios much higher than those possible in conventional compressors with comparable tip speeds. For comparison the design pressure ratio of the two-stage compressor is approximately equivalent to that of a six- or seven-stage conventional high speed compressor. Therefore, if the aspirated counter-rotating compressor could be successfully integrated in a gas turbine engine it would lead to a significantly smaller and lighter device.

6.1 Compressor Design Summary

The (absolute) tip speed chosen for both rotors was 457m/s (1500ft/s) which is typical of high-speed compressors. The blade rows were designed to produce optimal pressure distributions within diffusion factor and inlet Mach number constraints. For the aspirated blades, the diffusion factor limit is about 0.7, as opposed to 0.5 for conventional blades. The Mach number limit was chosen to be around 1.5 to avoid large losses. This is important for high speed aspirated blades for which the shock losses can be up to 7 to 8 times larger than the viscous losses. The exit angle from the first stator was optimised to maximise the pressure ratio of the downstream (counter-rotating) rotor within the given constraints.

The initial flowpath shape was generated from a meanline analysis and then refined using the results of axisymmetric throughflow computations. The most distinctive feature of the flowpath is the large contractions across the rotors which is necessitated by the high pressure ratios. The blade sections were designed with the quasi-three-dimensional cascade code MISES which allowed for precise design of each blade feature to match the flow conditions. MISES was also used to determine the optimum aspiration scheme for each blade section.

The overall pressure ratio of the final (MISES) design is about 9.1:1 (3.46:1 in stage 1 and 2.64:1 in stage 2). The maximum diffusion factor in the compressor is 0.75 at the tip of the first rotor. This section also has the highest suction requirement which is 2.1%. The maximum relative inlet Mach number is about 1.53 and occurs at the tip sections of both rotors.

6.2 Concluding Remarks on Design Process

Several important issues were addressed in the process of designing the aspirated counter-rotating compressor. These are significant to the design of high-speed aspirated stages and may prove significant to the design of other high-work stages as well. It was found in general that there is a high potential for complicated interaction between design features and aerodynamic behaviour. In this design, for example, the exit angle of the first stator and the diffusion factor of the downstream rotor exhibit a highly nonlinear interaction. This makes an iterative design process such as that used here (and by Merchant [18]) critical to obtaining a good final design.

A more specific issue addressed in the design process was that shock losses are as important as viscous losses (if not more so) to the efficiency of a high-speed aspirated stage. This dictates that equal attention should be paid to the relative inlet Mach numbers and diffusion factors of the blades in the stage design process. In some cases, it will be the Mach number and not the diffusion factor that will limit the design of a particular compressor feature. This is a notable difference from conventional compressors which have lower diffusion factor limits.

Given the large pressure ratios across high-work compressor stages, flowpath contraction also becomes an issue. This can significantly impact the performance of the compressor and poses a unique design challenge. In this design, it was necessary to depart from the common practice of holding the tip radius constant through the compressor and a great deal of effort was required to obtain a sufficiently smooth hub profile. A detailed throughflow analysis provides invaluable information on the impacts of flowpath shape on aerodynamic behaviour.

Design of blade sections for high-speed aspirated stages also involves some challenges. In particular, there is a strong interrelation between blade features which necessitates an iterative design process (generally involving many iterations). The features of the blades also differ in many respects from those of conventional blades. Despite this, some correlations between certain features of high-speed aspirated blades and some design trends were identified in this work. These are useful for obtaining a good starting point for the design of a blade section, so that ultimately fewer iterations are required to reach an optimal design.

6.3 Future Work

The next step in the process of designing the aspirated counter-rotating compressor will be to complete the three-dimensional computational aerodynamic analysis. This will provide information on the effects of tip clearance flows, radial transport, and mixing between blade rows and on the ability of the compressor to pass the design mass flow among other things. Based on this information, some modification of the design will likely be necessary. Three-dimensional computational analysis of such a high-performance compressor is, however, not straightforward. Initial attempts to complete such an analysis encountered several difficulties. It appears that very careful attention must be paid to the abilities of the computational tools and to the procedure used to carry out the computations.

Once the design of the compressor has been satisfactorily completed (including all relevant structural analysis), the next step will be to build and test the device. As mentioned previously the compressor could be tested in the Blowdown Compressor facility at MIT. Since this facility has been used in the past to test only single-stage, comparatively low-speed compressors, some issues with the setup would need to be addressed. Perhaps one of the most important is the accommodation of the second, counter-rotating stage. This would involve (among other things) lengthening the test section and adding a motor to drive the second rotor.

In order to integrate the aspirated counter-rotating compressor in an actual gas turbine engine, some redesign of other engine components will also be necessary. Most notably a counter-rotating turbine will be required to drive the compressor. Preliminary investigation of such a turbine showed that it will benefit aerodynamically from the counter-rotation (as the compressor does) and should be capable of producing the required power in few stages. This provides an additional contribution to the overall goal of producing a smaller, lighter engine.

Bibliography

[1] J.D. Anderson. *Modern Compressible Flow.* McGraw-Hill, 1990.

[2] L.R. Anderson, W.H. Heiser, and J.C. Jackson. Axisymmetric one-dimensional compressible flow - theory and applications. *Journal of Applied Mechanics*, pages 917–923, December 1970.

[3] N.A. Cumpsty. *Compressor Aerodynamics.* Addison Wesley Longman, 1989.

[4] M. Drela. Xfoil: An analysis and design system for low reynolds number airfoils. In *Low Reynolds Number Aerodynamics*, T.J. Mueller, editor, June 1989.

[5] M. Drela. A user's guide to MTFLOW 1.2, November 1997.

[6] M. Drela and M. Schafer. Experimental and computational investigation of divergant trailing edges. Technical Report CFDL TR-91-3, MIT CFD Laboratory, 1991.

[7] M. Drela and H.H. Youngren. A user's guide to MISES 2.53, December 1998.

[8] A. Epstein. 16.511 course notes. Department of Aeronautics and Astronautics, Massachusetts Institute of Technology, Fall 2000.

[9] J.H. Freedman. Design of a multi-spool, high-speed, counter-rotating, aspirated compressor. Master's thesis, Massachusetts Institute of Technology, 2000.

[10] J.L. Kerrebrock. *Aircraft Engines and Gas Turbines.* MIT Press, Cambridge, 1996.

[11] J.L. Kerrebrock, M. Drela, A.A. Merchant, and B.J. Schuler. A family of designs for aspirated compressors. Technical Report 98-GT196, ASME, 1998.

[12] J.L. Kerrebrock, D.P. Reijnen, W.S.Ziminsky, and L.M. Smilg. Aspirated compressors. Technical Report 97-GT525, ASME, 1997.

[13] C.C. Koch and L.H. Smith Jr. Loss sources and magnitudes in axial-flow compressors. *Journal of Engineering for Power*, pages 411–424, July 1976.

[14] C.H. Law and A.J. Wennerstrom. Performance of two transonic compressor rotors incorporating inlet counterswirl. *Journal of Turbomachinery*, 109:142–148, January 1987.

[15] S. Lieblein, F.C. Schwenk, and F.L. Broderick. Diffusion factor for estimating losses and limiting blade loadings in axial flow compressor blade elements. Technical Report RME53D01, NACA, 1953.

[16] J.D. Mattingly. *Elements of Gas Turbine Propulsion.* McGraw-Hill, 1996.

[17] A.A. Merchant. Design and analysis of supercritical airfoils with boundary layer suction. Master's thesis, Massachusetts Institute of Technology, 1996.

[18] A.A. Merchant. *Design and Analysis of Axial Aspirated Compressor Stages.* PhD thesis, Massachusetts Institute of Technology, 1999.

[19] D.P. Reijnen. *Experimental Study of Boundary Leyer Suction in a Transonic Compressor.* PhD thesis, Massachusetts Institute of Technology, 1997.

[20] E.J. Sabel and A. Sabatiuk. Turbojet engine development: Design of phase 1 compressor. Technical Report 501, Curtis-Wright Corporation, 1957.

[21] B.J. Schuler. *Experimental Investigation of an Aspirated Fan Stage.* PhD thesis, Massachusetts Institute of Technology, 2001.

[22] B.J. Schuler, J.L. Kerrebrock, A.A. Merchant, and M. Drela. Design, analysis, fabrication and test of an aspirated fan stage. Technical Report 2000-GT618, ASME, 2000.

[23] A.J. Wennerstrom. Design of critical compressor stages. In *Transonic Compressors*, Volume 2, von Karman Institute Lecture Series 1988-03, 1988.

[24] A.J. Wennerstrom. Highly loaded axial flow compressors: History and current developments. *Journal of Turbomachinery*, pages 567–578, October 1990.

[25] H.H. Youngren and M. Drela. Viscous/inviscid method for preliminary design of transonic cascades. Technical Report 91-2364, AIAA, 1991.

Appendix A

25% and 75% Span Blade Sections

The 25% and 75% span section designs for each blade row are given below. For each section the blade shape, surface isentropic Mach number distribution, and pressure contours are shown.

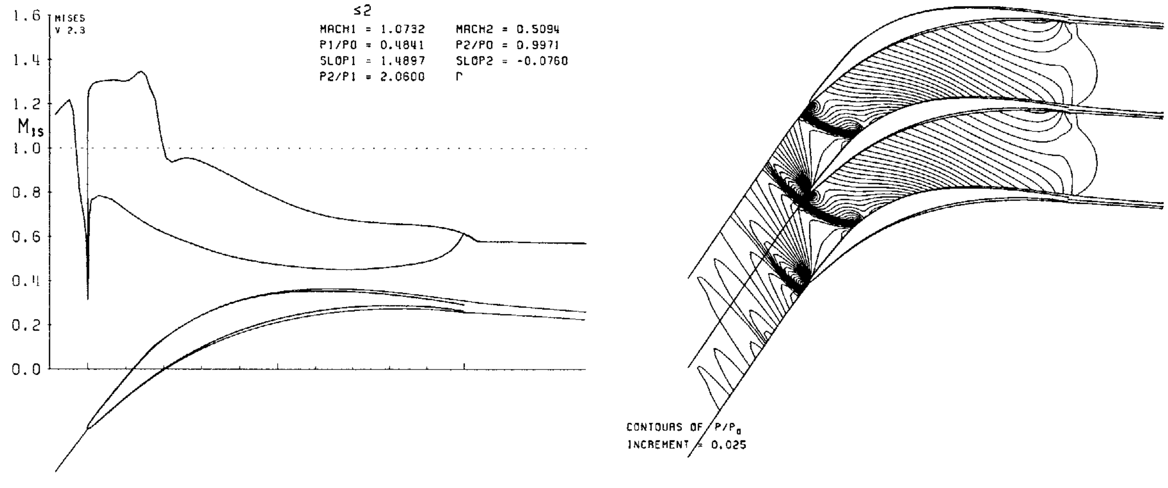

(a) Blade shape & Mach number

(b) Pressure contours

Figure A-1: Rotor 1 25% Span

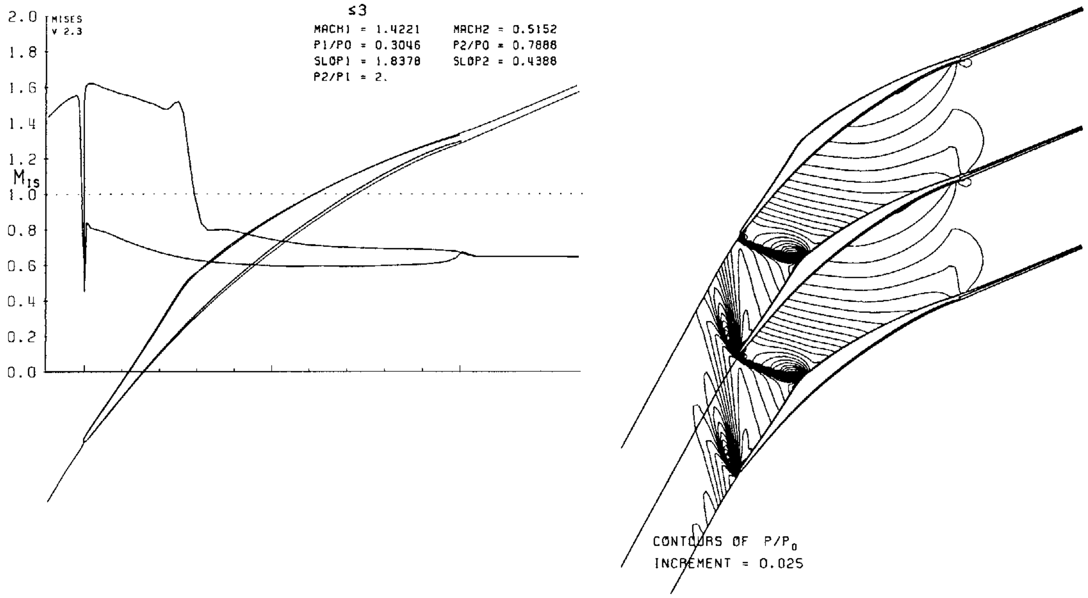

(a) Blade shape & Mach number (b) Pressure contours

Figure A-2: Rotor 1 75% Span

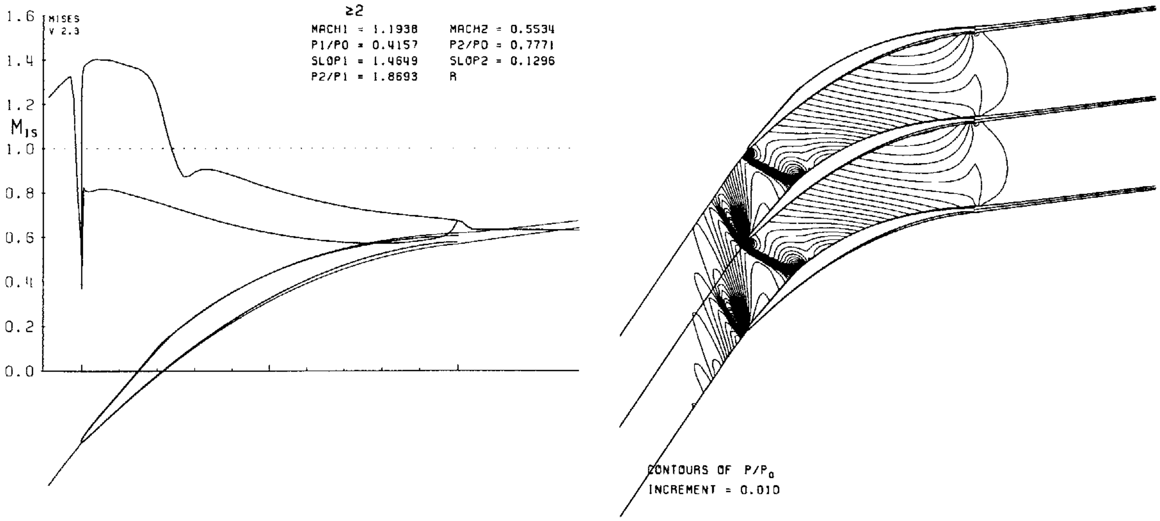

(a) Blade shape & Mach number (b) Pressure contours

Figure A-3: Stator 1 25% Span

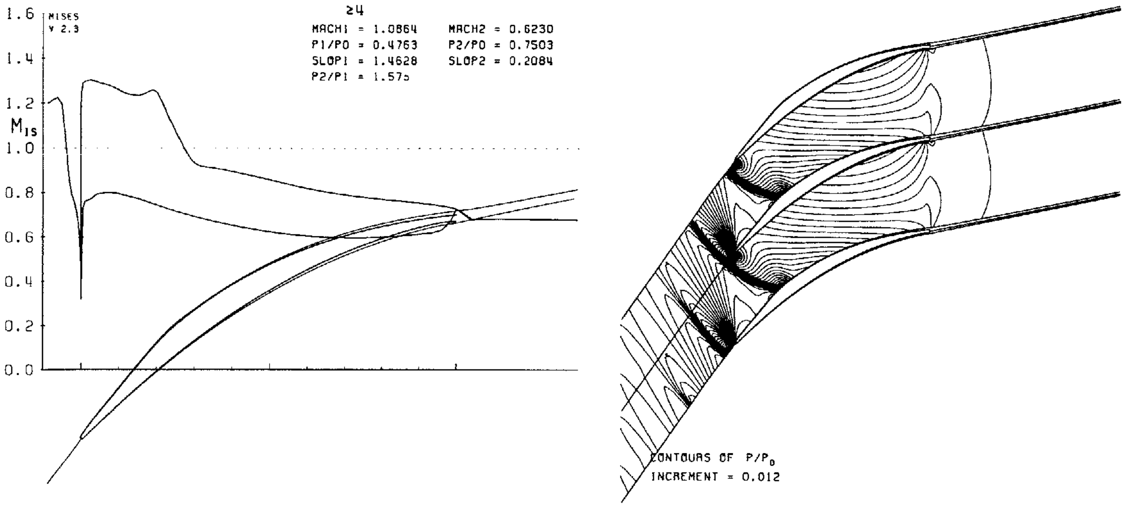

(a) Blade shape & Mach number (b) Pressure contours

Figure A-4: Stator 1 75% Span

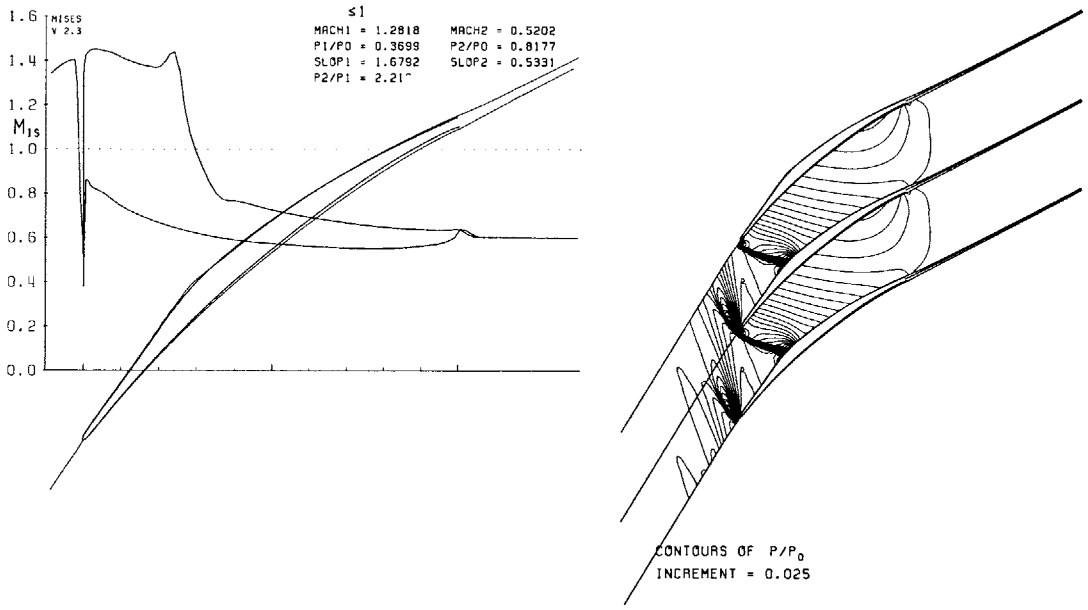

(a) Blade shape & Mach number (b) Pressure contours

Figure A-5: Rotor 2 25% Span

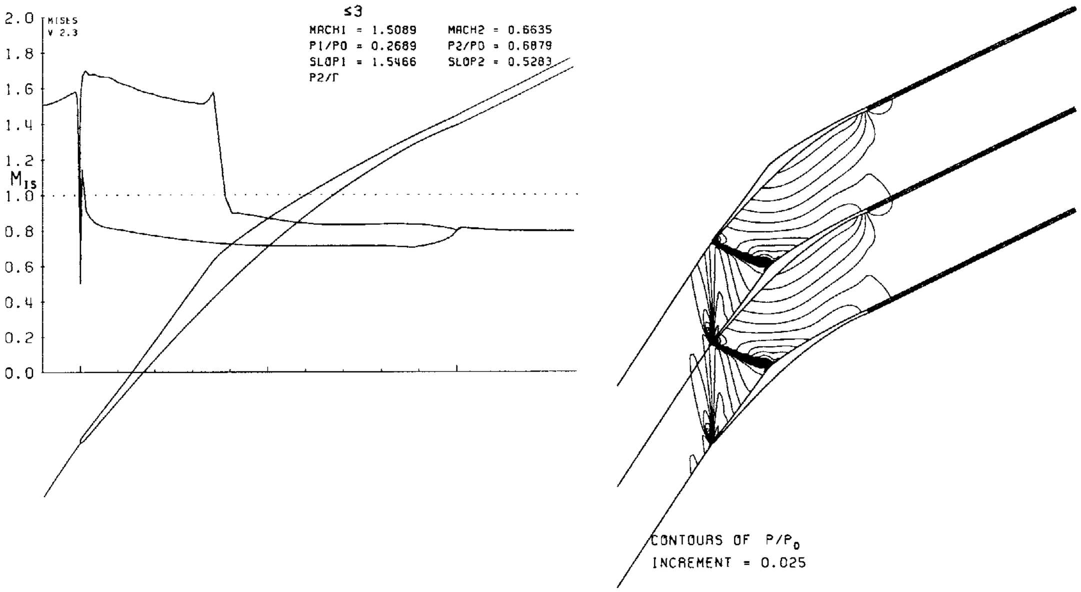

(a) Blade shape & Mach number (b) Pressure contours

Figure A-6: Rotor 2 75% Span

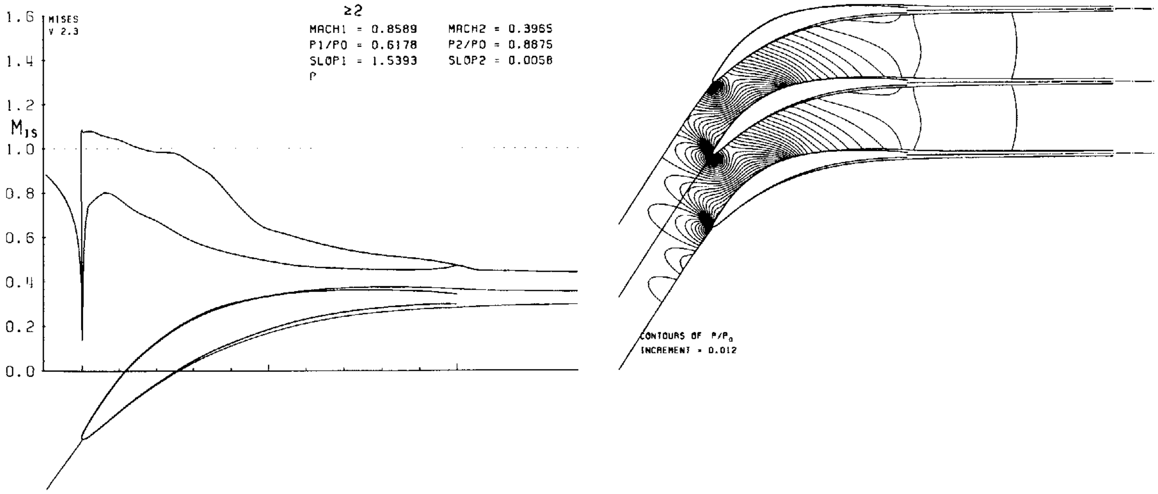

(a) Blade shape & Mach number (b) Pressure contours

Figure A-7: Stator 2 25% Span

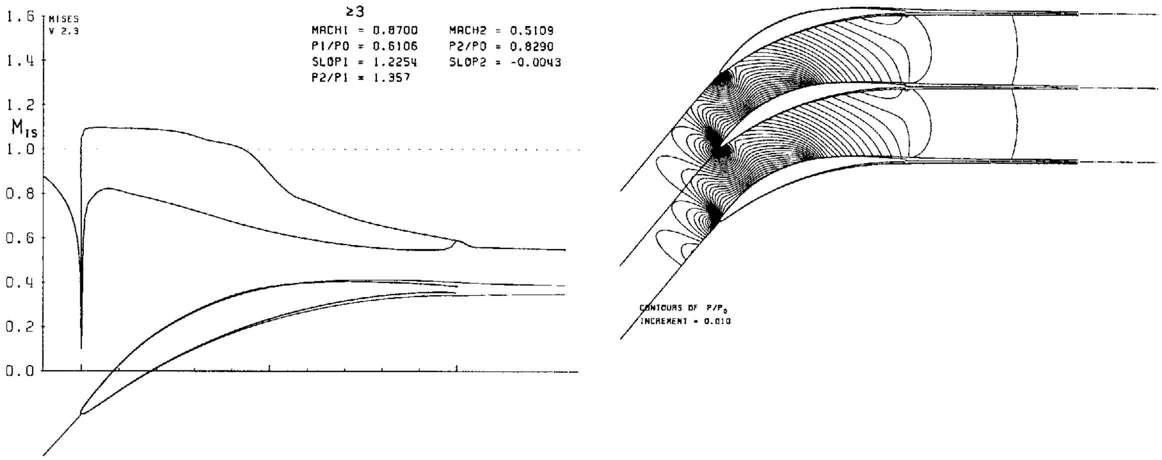

(a) Blade shape & Mach number (b) Pressure contours

Figure A-8: Stator 2 75% Span